Fast-slow analysis of passive mitigation of self-sustained oscillations by means of a bistable nonlinear energy sink

Baptiste Bergeot, Sébastien Berger

▶ To cite this version:

Baptiste Bergeot, Sébastien Berger. Fast-slow analysis of passive mitigation of self-sustained oscillations by means of a bistable nonlinear energy sink. 2023. hal-04280444v1

HAL Id: hal-04280444
https://hal.science/hal-04280444v1

Preprint submitted on 11 Nov 2023 (v1), last revised 3 Feb 2024 (v2)

Fast-slow analysis of passive mitigation of self-sustained oscillations by means of a bistable nonlinear energy sink

Baptiste Bergeot[a,*], Sébastien Berger[a]

[a]*INSA CVL, Univ. Orléans, Univ. Tours, LaMé EA 7494, F-41034, 3 Rue de la Chocolaterie, CS 23410, 41034 Blois Cedex, France*

Abstract

This paper investigates the dynamic behavior of a Van der Pol oscillator (used as an archetypal self-sustained oscillator) coupled to a bistable nonlinear energy sink (BNES). We first show using numerical simulations that this system can undergo a multitude of motions including different types of periodic regimes and so-called strongly modulated responses (SMR) as well as chaotic regimes. We also show that a BNES can be much more efficient than a classical cubic NES but this is not robust since a little perturbation can switch the system from harmless to harmful situations. However, even in the most unfavorable cases, it is possible to find a set of parameters for which the BNES performs better than the NES.

A multiple time scales approach is then addressed to analyze the system. In this context, we show that the so-called Multiple Scale/Harmonic Balance Method (MSHBM) must be modified (compared to its usual use) to consider the specific feature of the BNES, i.e., that it can have a nonzero-mean oscillating motion. This allows us to derive a so-called amplitude-phase modulation dynamics (APMD) which can reproduce the complex behavior of the initial system. Because of the presence of a small perturbation parameter (i.e., the mass ratio between the BNES and the VdP oscillator), the APMD is governed by two different time scales. More precisely, it appears as a (3,1)-fast-slow system whose motion is constituted in a succession of slow and fast epochs. Founding a (3,1)-fast-slow APMD is interesting since that implies a more complex dynamics than in the case of a classic NES whose APMD is only (2,1)-fast-slow. A fast-slow analysis is finally conducted within the framework of the geometric singular perturbation theory. From the computation of the so-called critical manifold and the analytical expressions of the APMD fixed points, a global stability analysis is performed. This enables us to interpret a certain number of regimes observed on numerical simulations of the initial system.

Keywords: Passive vibration control, Bistable nonlinear energy sink, Self-sustained oscillations, Fast-slow analysis, Critical manifold

---

1. Introduction

The well-known nonlinear energy sinks (NESs) are nonlinear vibration absorbers used for passive mitigation of unwanted oscillations caused by either free, external, parametric or self-

---

[*] Corresponding author

Email addresses: `baptiste.bergeot@insa-cvl.fr` (Baptiste Bergeot), `sebastien.berger@insa-cvl.fr` (Sébastien Berger)

excitations of a mechanical or acoustical system referred to as the primary structure. In most cases, an NES is a light mass (compared to the total mass of the primary structure) nonlinear attachment consisting of an essentially nonlinear spring (most of the time purely cubic) and a viscous linear damper. The dependence between the vibratory amplitude and the oscillating frequency of the NES (because of its strongly nonlinear nature) makes it able to resonate at any frequency. After tuning to the primary structure and absorbing and dissipating its energy, the NES can detune to prevent the energy from returning. This irreversible transfer of vibrational energy from the primary structure to the NES is called targeted energy transfer (TET) or energy pumping to the primary structure. In the seminal papers by Gendelman, Vakakis *et al.* [1, 2] the TET phenomenon is explained by the interaction between two nonlinear normal modes of vibration of the system producing a 1:1 resonance capture. Reviews of these concepts can be found in [3].

More recently, the bistable NES (BNES) consisting of a small mass connected to the primary structure by a spring with a negative linear stiffness and a nonlinear (cubic) stiffness [4, 5] has been introduced. These negative linear and nonlinear stiffness components can be realized for example through the geometric nonlinearity of the transverse displacement of pre-compressed linear springs [6] or considering the transverse vibration of a thin viscously damped fixed-fixed beam with a small mass fixed at its centre when buckled under axial constraint [7, 8, 9]. Most studies about BNESs consider either mitigation of free vibrations or vibrations caused by external harmonic forcing. The seminal papers [4, 5] relate to mitigation of free vibrations. Romeo *et al.* shows that BNES can produce TET even at low energies, in contrast to the classic cubic NESs. From an analytical method, Habib and Romeo [10] propose a procedure to tune and optimize a BNES to mitigate free vibration of a two-degree-of-freedom (2-dof) primary structure. Dekemele *et al.* [11] present an analytical study of the tuning and the performance of a BNES again in the context of mitigation of free vibrations. Mattei *et al.* [7] and Iurasov and Mattei [8] study both numerically and experimentally the mitigation of forced vibrations by a beam-based BNES. An adapted semi-analytical method to predict the energy pumping time of a BNES under harmonic forcing is proposed by Wu *et al.* [12]. The vibration reduction performance of a BNES and an NES is compared, by Wand *et al.* [13] and the results show that the BNES performs over the full frequency band.

Using a cubic NES to mitigate limit cycle oscillations (LCOs) resulting from dynamic instabilities has been extensively studied in the literature. Mitigation of LCOs of the Van der Pol oscillator has been studied numerically by Lee *et al.* in their seminal paper [14] and then analytically by Gendelman and Bar [15]. A number of works focus on mitigation of flutter instabilities in aircraft wings. This problem has been first studied both numerically and experimentally, again by Lee. *et al.* [16, 17, 18]. The theoretical prediction of observed operating regimes has been performed by means of multiple time scales approaches [19, 20] and improved more recently using the center manifold reduction technique [21]. The possibility of mitigating self-sustained oscillations of a linear friction system having two unstable modes has been studied by Bergeot *et al.* [22] by means of a sophisticated multiple time scales analysis allowing the understanding of the phenomena underlying the appearance of the many possible regimes of the system. Effect of stochastic forcing on the dynamic behavior of a self-sustained oscillator coupled to a nonlinear energy sink has been investigated in [23]. On the contrary, the use of a BNES to mitigated self-sustained vibrations is poorly addressed in the literature. To the best of the authors' knowledge, the only paper dealing with this subject is by Franzini et al. [24]. It presents numerical and analytical studies for a BNES-based device used to simultaneously alleviate the unwanted vibrations caused by a galloping phenomenon and perform electro-mechanical energy conversion by the piezoelectric effect.

In general, when an NES is attached to a primary structure, the resulting coupled model is analyzed by introducing a small perturbation parameter related to the mass ratio between the NES and the primary structure. It is customary to study the dynamic behavior of the system in the neighborhood of this 1:1 resonance capture. In general, the system is simplified by averaging it over a natural period of the primary structure using the so-called Complexification-Averaging Method (CAM) [25, 3] or the Multiple Scale/Harmonic Balance Method (MSHBM) [26, 27]. The resulting system, called here *amplitude-phase modulation dynamics*[1] (APMD), is then analyzed by means of singular perturbation techniques (by multiple scales methods [28] or geometric singular perturbation theory [29]). The first key point of these analytical processes is the partitioning of the APMD into two time scales (one slow and one fast[2]). In this representation the time evolution of the APMD is thus described as a succession of slow and fast epochs which are analyzed independently. The second key point is the definition of the so-called *critical manifold*[3] whose system trajectories converge during slow epochs.

Some of the work mentioned above on the analytical study of energy pumping by a BNES follows this multiple time scales based methodology (or fast-slow analysis). However, in these studies, the CAM (or MSHBM) is used in the same way as if we were considering a classical NES, i.e., assuming that the BNES motion has the form of a zero-mean oscillating regime. This forgets one essential feature a bistable system motion, it can have a nonzero-mean. The resulting analysis can therefore only partially explain the dynamic behavior of the system, in particular for chaotic and intra-well motions of the BNES.

In the present paper, the MSHBM is used and modified (compared to its usual use) to take into account a nonzero-mean motion. This allows us to obtain an APMD and a critical manifold that can explain numerous regimes observed in numerical simulations of a Van der Pol oscillator (used as an archetypal self-sustained oscillator) coupled to a BNES.

The paper is organized as follows. In Section 2, the equations of motion of the full-order system under study - i.e. a Van der Pol oscillator coupled to a BNES - are obtained. Then, the dynamic behavior of a Van der Pol oscillator coupled to a BNES is investigated by means of numerical simulations. Using the MSHBM, the equations of the APMD are derived in Section 3. The fast-slow analysis of the APMD is detailed in Section 4. That allows us to perform a asymptotic global stability analysis in Section 5, which enables us to understand the observed behavior using numerical simulations. Finally, concluding remarks and perspectives are formulated in Section 6.

2. Equations and dynamic behavior of the model

2.1. Equations of motion of a Van der Pol oscillator coupled to a BNES

In this section we derive the equations of motion of the full-order system under study, i.e. a Van der Pol (VdP) oscillator - used as an archetypal self-sustained oscillator - coupled to an ungrounded

---

[1] Most of the time authors name it the *slow flow dynamics*. It is named here in the manner of Luongo and Zulli [26, 27] to avoid vocabulary ambiguities.

[2] Sometimes the terms “slow” and “super-slow” [15, 30] are used to leave the term “fast” for the oscillations on which the averaging was carried out and therefore to be coherent with the term slow flow. In the present work the terms “slow” and “fast” are preferred to be in agreement with the vocabulary usually used in the literature on dynamical systems.

[3] The critical manifold is also called *slow invariant manifold* in the literature.

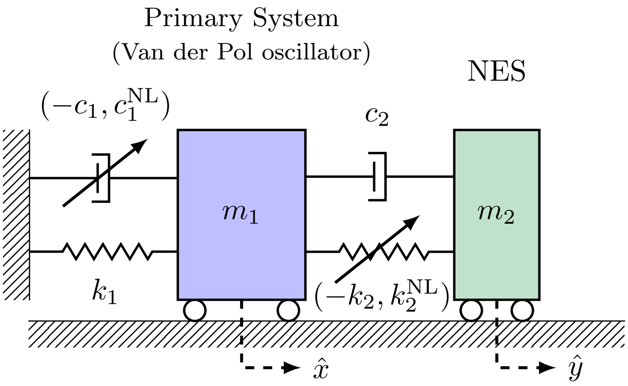

Figure 1: A Van der Pol oscillator coupled to a BNES.

bistable nonlinear energy sink (BNES). The BNES consists in a mass coupled to a linear damper and to a spring with a negative stiffness and a cubic stiffness. A schematic representation of this system is shown in Fig. 1. The equations of motion of this system, with respect to the physical time $\hat{t}$, are as follows

$$\begin{aligned} m_1 \frac{d^2\hat{x}}{d\hat{t}^2} - c_1 \frac{d\hat{x}}{d\hat{t}} + c_1^{\mathrm{NL}} \frac{d\hat{x}}{d\hat{t}} \hat{x}^2 + k_1 \hat{x} + \\ c_2 \left(\frac{d\hat{x}}{d\hat{t}} - \frac{d\hat{y}}{d\hat{t}} \right) - k_2 \left(\hat{x} - \hat{y} \right) + k_2^{\mathrm{NL}} \left(\hat{x} - \hat{y} \right)^3 = 0 \qquad \text{(1a)} \end{aligned}$$

$$m_2 \frac{d^2\hat{y}}{dt^2} + c_2 \left(\frac{d\hat{y}}{d\hat{t}} - \frac{d\hat{x}}{d\hat{t}} \right) - k_2(\hat{y} - \hat{x}) + k_2^{\mathrm{NL}} (\hat{y} - \hat{x})^3 = 0 \qquad \text{(1b)}$$

where m_1 and m_2 are the masses of the primary VdP oscillator and of the BNES, respectively. The parameter k_1 is the linear stiffness of the VdP oscillator and $-c_1$ (with $c_1 > 0$) and c_1^{NL} characterize its linear negative and nonlinear dampings, respectively. The BNES is characterized by its linear damping coefficient c_2, negative linear stiffness $-k_2$ (with $k_2 > 0$) and nonlinear stiffness k_2^{NL}.

Equation (1) is rescaled leading to the following dimensionless system of differential equations

$$\begin{aligned} \ddot{x} - \epsilon\sigma\dot{x} + \epsilon\lambda\dot{x}x^2 + x + \\ \epsilon\mu \left(\dot{x} - \dot{y} \right) - \epsilon\beta(x - y) + \epsilon\alpha(x - y)^3 = 0 \qquad \text{(2a)} \end{aligned}$$

$$\epsilon\ddot{y} + \epsilon\mu \left(\dot{y} - \dot{x} \right) - \epsilon\beta(y - x) + \epsilon\alpha(y - x)^3 = 0 \qquad \text{(2b)}$$

where $x = \hat{x}/L$, $y = \hat{y}/L$ (with L a characteristic length of the motion), $\omega_1 = \sqrt{k_1/m_1}$, $t = \omega_1 \hat{t}$, $\dot{\{\}} = d\{\}/dt$, $\epsilon = m_2/m_1$ is the mass ratio between the NES and the VdP oscillator, $\sigma = c_1/(m_2\omega_1)$, $\lambda = c_1^{\mathrm{NL}} L^2/(m_2\omega_1)$, $\mu = c_2/(m_2\omega_1)$, $\beta = k_2/(m_2\omega_1^2)$ and $\alpha = k_2^{\mathrm{NL}} L^2/(m_2\omega_1^2)$.

The static solutions of Eq. (2) are: the trivial solution

$$p_0^{\mathrm{st}} = (x_0^{\mathrm{st}}, y_0^{\mathrm{st}}) = (0, 0) \qquad (3)$$

which is unstable and the two following non trivial solutions

$$p_1^{\mathrm{st}} = (x_1^{\mathrm{st}}, y_1^{\mathrm{st}}) = \left(0, \sqrt{\frac{\beta}{\alpha}} \right) \quad \text{and} \quad p_2^{\mathrm{st}} = (x_2^{\mathrm{st}}, y_2^{\mathrm{st}}) = \left(0, -\sqrt{\frac{\beta}{\alpha}} \right). \qquad (4)$$

which are stable if there are no self-sustained oscillations. For a classic cubic NES, i.e., $\beta = 0$, the only equilibrium position is p_0^{st} which is stable (again if there are no self-sustained oscillations).

Finally, for comparison purposes, we give here an approximated solution of the VdP oscillator uncoupled from the NES whose equation of motion is $\ddot{x} - \epsilon\sigma\dot{x} + \epsilon\lambda\dot{x}x^2 + x = 0$. This approximated solution is obtained using the Krylov-Bogoliubov method of averaging (see e.g. [31]) as

$$x(t) = \underbrace{\frac{2\sqrt{\sigma}e^{\frac{\sigma t\epsilon}{2}}}{\sqrt{\frac{4\sigma}{r_0^2} + \lambda\left(e^{\sigma t\epsilon} - 1\right)}}}_{r(t)} \cos(t + \varphi_0) \tag{5}$$

where φ_0 is the phase at the origin of time. Details on obtaining Eq. (5) are given in Appendix A. For $\lambda > 0$, the amplitude $r(t)$ in Eq. (A.8) tends to zero if $\sigma < 0$ and to $2\sqrt{\frac{\sigma}{\lambda}}$ if $\sigma > 0$. In other words, for the original VdP oscillator (A.1), if $\sigma < 0$ the trivial solution $(x, \dot{x}) = (0, 0)$ is stable and becomes unstable when $\sigma > 0$. The periodic solution

$$(x, \dot{x}) = \left(2\sqrt{\frac{\sigma}{\lambda}}\cos(t + \varphi_0), -2\sqrt{\frac{\sigma}{\lambda}}\sin(t + \varphi_0)\right) \tag{6}$$

exists and it is stable for $\sigma > 0$.

2.2. Response regimes of a Van der Pol oscillator coupled to a BNES

In this section, the dynamic behavior of a Van der Pol oscillator coupled to a BNES is presented by means of direct numerical integration of Eq. (2).

We first recall briefly the response regimes observed when an NES (i.e., with no linear stiffness) is used instead of a BNES. As it is widely discussed in the literature (see e.g. [15, 19]), in this case, four scenarios are observed. In previous works by the authors [32, 33] these responses are sorted into two categories. In the first category, the NES acts, resulting in three responses called *harmless situations*. These three harmless regimes are: (i) the *complete suppression* in which the trivial equilibrium is stabilized because of the additional linear part of the NES including mass and damping; (ii) the *mitigation through periodic responses (PRs)* with an amplitude smaller than the periodic response undergone by the VdP oscillator alone and (iii) the *mitigation through a Strongly Modulated Response (SMR)* corresponding to a quasi-periodic (amplitude and phase modulated) regime again with a maximum amplitude smaller than the periodic response undergone by the VdP oscillator alone. In the second category, the NES does not act, resulting in a *no mitigation response* called *harmful situation*. In this case a periodic regime with an amplitude close to what is observed when the VdP oscillator is not coupled to the NES. The specific value of the bifurcation parameter σ at which the system switches from a harmless regime to a harmful regime is called the *mitigation limit* of the NES, denoted as σ_{ml}. In the case of an NES the mitigation limit is defined considering a set of initial conditions (for the slow flow) as a small perturbation of the trivial equilibrium solution, i.e., $(x_0^{\text{st}}, y_0^{\text{st}}) = (0, 0)$.

The specific features of a BNES compared with an NES are presented first in Fig. 2 in which, as a function of σ, the steady-state maximum amplitude of the VdP oscillator alone is compared to the steady-state maximum amplitude of the VdP oscillator coupled to an NES on the one hand and to a BNES on the other. The following set of parameters is used:

$$\text{VdP parameter:} \quad \lambda = 0.5 \tag{7a}$$

$$\text{BNES parameters:} \quad \mu = 0.06, \quad \beta = 0.575, \quad \alpha = 2, \tag{7b}$$

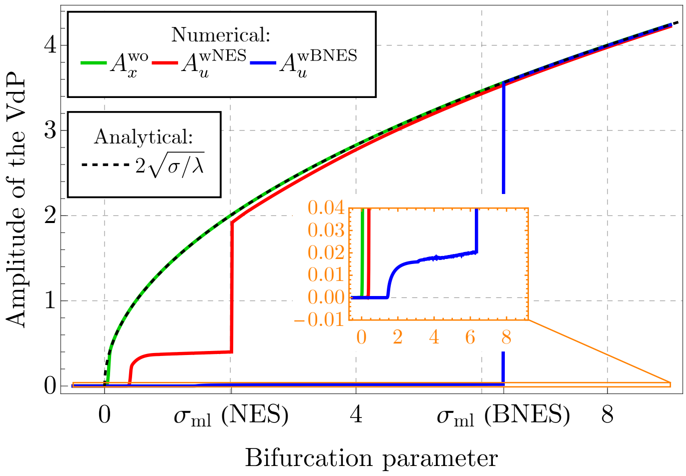

Figure 2: Steady-state maximum amplitude of the VdP oscillator alone A_x^{wo} (green) compared to the steady-state maximum amplitudes A_x^{wNES} and A_x^{wBNES} of the VdP oscillator coupled to an NES (red) and to a BNES (blue), respectively, as functions of the bifurcation parameter σ. The theoretical amplitude of the VdP alone (see Eq. (6)) is also displayed (black dashed). Parameters: (7a) are used to compute A_x^{wo} from Eq. (A.1); (7a) with $\mu = 0.4$, $\beta = 0$ are used to compute A_x^{wNES} from Eq. (2) and (7) are used to compute A_x^{wBNES} also from Eq. (2).

The steady-state maximum amplitude of the VdP oscillator alone is defined as follows

$$A_x^{\mathrm{wo}} = \frac{\max[(x(0.9T), x(T))] - \min[(x(0.9T), x(T))]}{2} \tag{8}$$

where $x(t)$ is the time series of the variable x computed by means of the numerical integration of Eq. (A.1) from $t = 0$ to $t = T$ and using the parameters (7a). In a similar way, the steady-state maximum amplitude of the VdP oscillator coupled to an NES is

$$A_x^{\mathrm{wNES}} = \frac{\max[(x(0.9T), x(T))] - \min[(x(0.9T), x(T))]}{2} \tag{9}$$

where $x(t)$ is the time series of the variable x computed by means of the numerical integration of Eq. (2) with $\mu = 0.4$, $\beta = 0$ and $\alpha = 2$ (case of an NES with good properties of mitigation) and using the VdP parameters (7b). Finally, the steady-state maximum amplitude of the VdP oscillator coupled to a BNES is

$$A_x^{\mathrm{wBNES}} = \frac{\max[(x(0.9T), x(T))] - \min[(x(0.9T), x(T))]}{2} \tag{10}$$

where $x(t)$ is the time series of the variable u computed by means of the numerical integration of Eq. (2) using the parameters (7) (case of an NES with good properties of mitigation).

The theoretical amplitude of the VdP alone (see Eq. (6)) is also displayed in Fig. 2. We can first see that the mitigation limit of the BNES ($\sigma_{\mathrm{ml}} \approx 6.35$) is higher than that of the NES ($\sigma_{\mathrm{ml}} \approx 2$). Secondly, in cases of attenuation (PRs or SMRs, the difference between these two regimes is not visible in the figure: from $\sigma \approx 0.4$ to $\sigma \approx 3$ for the NES and from $\sigma \approx 1.75$ to $\sigma \approx 7.86$ for the BNES) the maximum amplitude A_x^{wBNES} is almost 10 times smaller than A_x^{wNES}. This last observation is of course interesting from the point of view of vibration attenuation, but we shall see that it can have a negative impact on the robustness of the BNES.

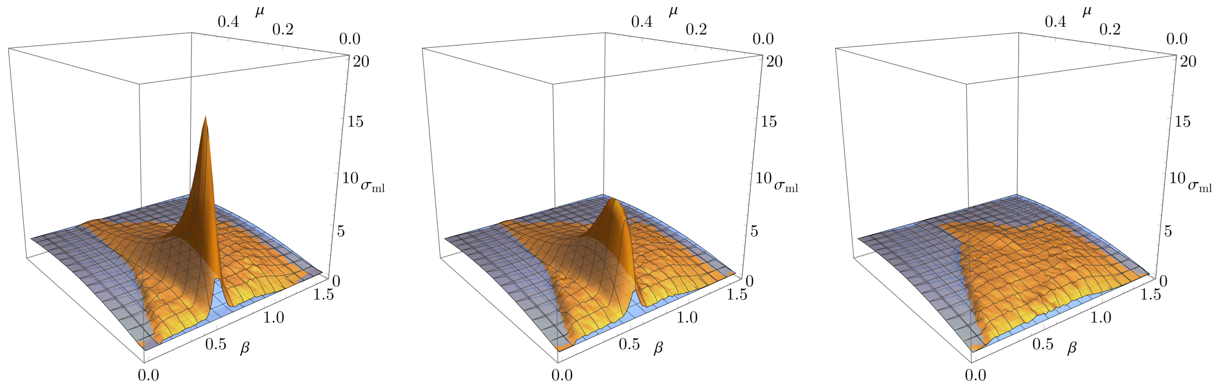

(a) (b) (c)

Figure 3: Mitigation limit $\sigma_{\rm ml}$ as a function of β and μ in the case of an NES (blue surface) and a BNES (orange surface) for λ given by (7a), $\alpha = 2$ and $\epsilon = 0.0025$. The initial conditions are $p_0^{\rm st} + (per, per)$ for the NES and $p_1^{\rm st} + (per, per)$ for the BNES, respectively. The perturbation parameter is 0.001, 0.01 and 0.1 in (a) to (c), respectively.

How large is the perturbation does not really matter in the case a classic purely cubic NES. This is not the case for a BNES. To show this, Fig. 3 plots the the mitigation limit $\sigma_{\rm ml}$ as a function of β and μ in the case of an NES and a BNES for λ given by (7a), $\alpha = 2$ and $\epsilon = 0.0025$. The initial conditions are $p_0^{\rm st} + (per, per)$ for the NES and $p_1^{\rm st} + (per, per)$ for the BNES, respectively. The perturbation value is 0.001, 0.01 and 0.1 in Figs. 3(a) to 3(c), respectively. The mitigation limit $\sigma_{\rm ml}$ is computed by locating the jumps on amplitude profiles such as those shown in Fig. 2. In the latter, results have been obtained in the same way with $per = 0.001$.

As mentioned above, the mitigation limit of the NES (in blue color in Fig. 3) is not affected by the change in initial conditions and of course it does not depend on β. On the contrary, the mitigation limit of the BNES (in orange color in Fig. 3) it is greatly affected by the change in initial conditions. Indeed, a very high maximum is present when per is small. This maximum decreases until it disappears when per increases. That shows that the BNES can be very efficient but this is not robust since a little perturbation can switch the system from harmless to harmful situations. However, even in the case of $per = 0.1$ (see Fig. 3(c)) it is possible to find a set of parameters for which the BNES performs better than the NES.

The overall results of Fig 3, in terms of mitigation limit, do not highlight the complex dynamic behavior of the BNES. As in the case of a classic NES, when $\sigma > \sigma_{\rm ml}$ the system (2) undergoes a periodic regime with an amplitude for the variable x close the that of the VdP oscillator alone. However, when $\sigma < \sigma_{\rm ml}$ a multitude of harmless regimes can be observed, whereas there are only four responses in the case of an NES. In Fig. 4, seven of these regimes are presented. The figure shows the time series $y(t)$ obtained from the numerical simulation of Eq. (2) and only steady states are shown. The equilibrium positions $y_1^{\rm st}$ and $y_2^{\rm st}$ (see Eq. (4)) are also depicted. The parameters used are $\lambda = 0.5$, $\alpha = 2$ (as in Fig. 3) and those given in Tab. 1. The initial conditions are the same as in Fig. 3(a), i.e, with $per = 0.001$. From Fig. 4(a) to Fig. 4(g) one has:

Fig. 4(a). The stabilization of $p_2^{\rm st}$.
Fig. 4(b). A PR centered on $y = 0$ (PR1).
Fig. 4(c). An SMR centered on $y = 0$ (SMR1).
Fig. 4(d). An intra-well (i.e., centered on $y = y_1^{\rm st}$) PR (PR2).

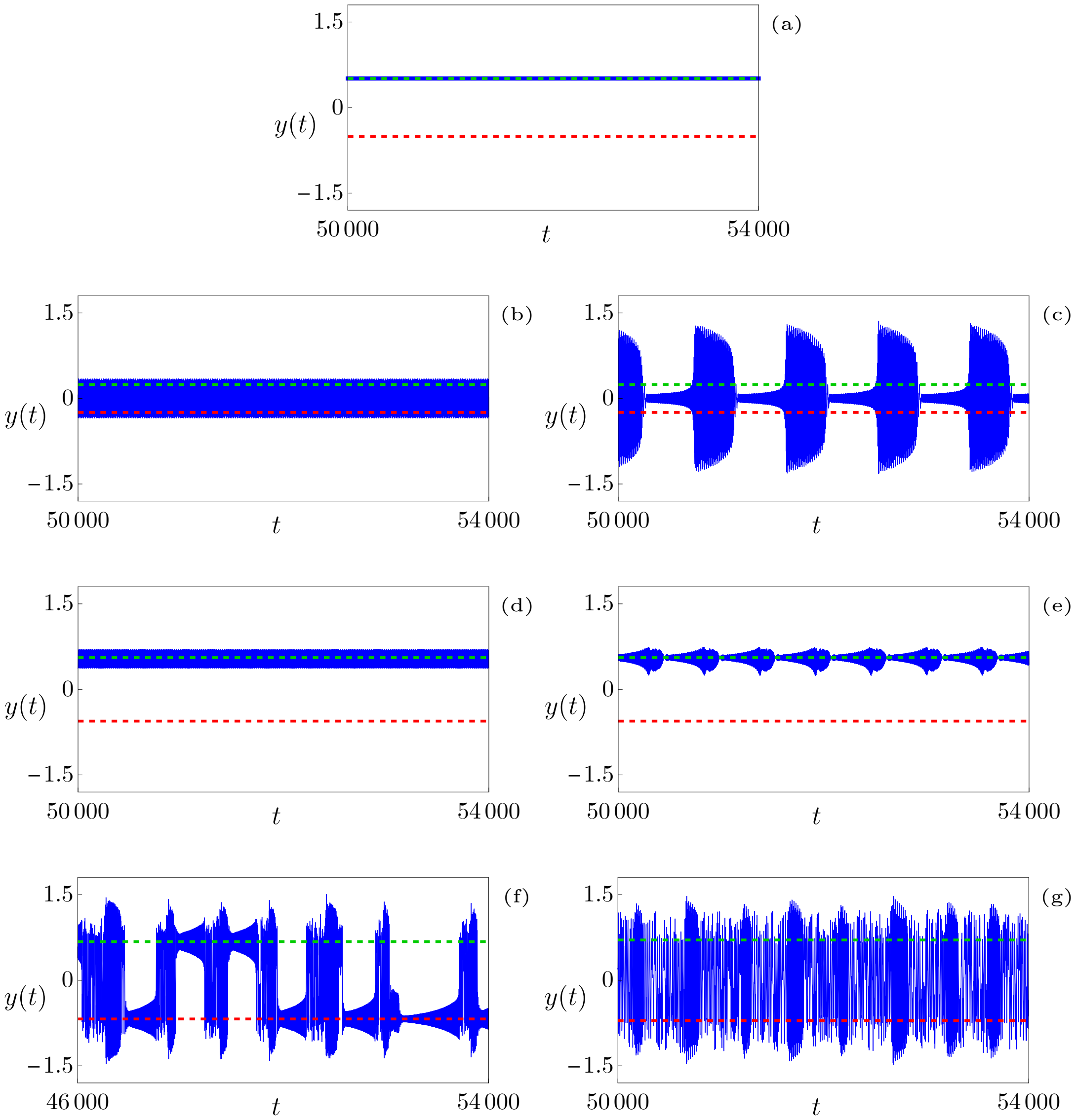

Figure 4: Time series $y(t)$ (solid blue line) obtained from the numerical simulation of Eq. (2), only steady states are shown. Equilibrium positions y_1^{st} (dashed green line) and y_2^{st} (dashed blue line). From (a) to (g) one has: (a) the stabilisation of p_2^{st} ; (b) a PR centered on $y = 0$; (c) an SMR centered on $y = 0$; (d) a PR centered on $y = y_2^{\text{st}}$; (e) an SMR centered on $y = y_2^{\text{st}}$; (f) an intermittent chaotic regime of type 1 (CR1), i.e., with a succession of oscillations centered on $y = 0$ and chaotic motions; and (g) an intermittent chaotic regime of type 2 (CR2), i.e., with succession of oscillations centered on $y = 0$, chaotic motions and oscillations centered on $y = y_1^{\text{st}}$ or $y = y_2^{\text{st}}$. The parameters used are $\lambda = 0.5$, $\alpha = 2$ and those given in Tab. 1. The initial conditions are the same as in Fig. 3(a), i.e, with $per = 0.001$.

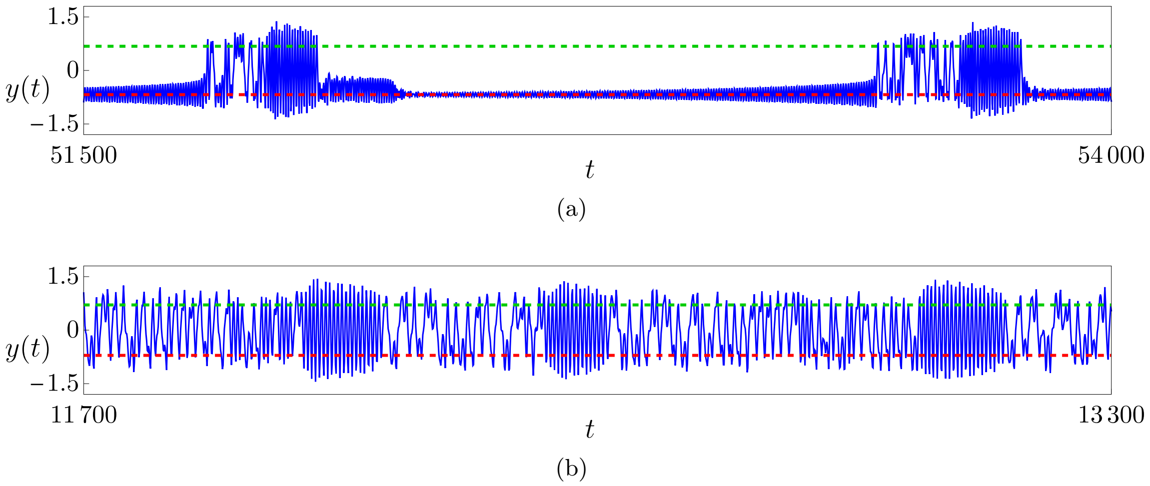

(a)

(b)

Figure 5: Zooms of (a) Figs. 4(f) and (b) 4(g).

Fig. 4(e). An intra-well SMR (SMR2);

Fig. 4(f). An intermittent chaotic regime of type 1 (CR1), i.e., with a succession of oscillations centered on $y = 0$, chaotic inter-well motions and oscillations centered on $y = y_1^{\mathrm{st}}$ or $y = y_2^{\mathrm{st}}$. A Zoom of Fig. 4(f) is shown in Fig. 5(a). On it, we can see first oscillations around $y = y_2^{\mathrm{st}}$, then a chaotic motion, then oscillations around zero and again oscillations around $y = y_2^{\mathrm{st}}$. Concerning these oscillations around $y = y_2^{\mathrm{st}}$, we first see amplitude-modulated oscillations that abruptly diminish to almost zero; after that we see oscillations with exponential growth before returning to a chaotic movement. The phase in which the oscillations around $y = y_2^{\mathrm{st}}$ (or also $y = y_1^{\mathrm{st}}$) are amplitude-modulated only rarely appears.

Fig. 4(g). An intermittent chaotic regime of type 2 (CR2), i.e., with a succession of oscillations centered on $y = 0$ and chaotic inter-well motions. This appears more clearly in Fig. 5(b) showing a Zoom of Fig. 4(g).

For regimes of Fig. 4(d) and (e), the motions observed are centered on y_1^{st} but similar regimes centered on $y = y_2^{\mathrm{st}}$ can also be observed depending on the chosen initial conditions. Regimes (a) to (c) are also observed with a classic cubic NES (of course in this case the stabilization concerns the trivial solution $y = y_0^{\mathrm{st}}$) while the regimes (d) to (g) are specific to BNES.

The maximum of σ_{ml} observed in Figs. 3(a) corresponds to a stabilization of the equilibrium $y = y_1^{\mathrm{st}}$ and $y = y_2^{\mathrm{st}}$ and for the other high efficient situations, the regimes observed just before σ_{ml} are the SMR2s or less often PR2s (for even smaller values of the perturbation parameter *per*, these two regimes with very small amplitudes can correspond to the highest values of σ_{ml}). Responses of type SMR2s are observed in the most efficient situations in the cases of Figs. 3(b) and 3(c). These observations will be interpreted after the fast-slow analysis carried out in Section. 4. Before that, the equation of the so-called *amplitude-phase modulation dynamics* are derived in the next section.

3. Equations of the amplitude-phase modulation dynamics

TET is due to the interaction between two nonlinear modes of the coupled structure [1, 2]. This phenomenon, called a 1:1 resonance capture, occurs at a frequency close to the natural frequency

Table 1: Parameters used for numerical simulations shown in Fig. 4. The corresponding values of σ_{ml} are also indicated.

	β	μ	σ	σ_{ml}
(a)	0.52	0.19	3.9	5.2
(b)	0.12	0.55	0.78	1.73
(c)	0.12	0.31	1.22	1.63
(d)	0.62	0.19	3.75	5
(e)	0.62	0.07	3.96	5.28
(f)	0.92	0.07	1.43	1.9
(g)	1	0.19	1.74	2.33

of the primary structure, here the VdP oscillator. It is customary to study the dynamic behavior of the system in the neighborhood of this 1:1 resonance capture. In general, the system is simplified by averaging it over a natural period of the primary structure using the so-called Complexification-Averaging Method (CAM) [25, 3]. The resulting averaged dynamics is called *amplitude-phase modulation dynamics* (APMD). The CAM is not consistent here due the bistable nature of the BNES, i.e., the fact that its motion can have a nonzero-mean. This is the reason why the Multiple Scale/Harmonic Balance Method (MSHBM) [26, 27] is preferred because it can easily and rigorously be modified (compared to its usual use) to take into account a nonzero-mean motion.

First, using the following change of variable

$$u = x + \epsilon \quad \text{and} \quad v = x - y \tag{11}$$

the equations of motion (2) become

$$\ddot{u} + u + \epsilon \left[-u - \sigma \dot{u} + \lambda \dot{u} u^2 + v \right] = 0 \tag{12a}$$

$$\ddot{v} + \mu \dot{v} - \beta v + \alpha v^3 + u = 0 \tag{12b}$$

Assuming a small mass ratio between the NES and the Van der Pol oscillator (i.e., $0 < \epsilon \ll 1$), only terms of order equal to 1 or less in ϵ have been kept in Eq. (12a). In Eq. (12b) keeping only the terms of order 0 is sufficient to correctly reproduce the essential characteristics of the dynamic behavior of the system.

Following the Multiple Scale Method (MSM) [31] the independent time variables $T_0 = t$, $T_1 = \epsilon t$, $T_2 = \epsilon^2 t$, ... are introduced. The time derivative rules are therefore $\frac{d}{dt} = D_0 + \epsilon D_1 + \epsilon^2 D_2 + \dots$ and $\frac{d^2}{dt^2} = D_0^2 + 2\epsilon D_0 D_1 + \epsilon^2 (D_0 D_2 + D_1^2) + \dots$ where $D_i = \frac{\partial}{\partial T_i}$ $(i = 0, 1, 2, \dots)$. The variables u and v are expanded in power series of ϵ as

$$u = u_0 + \epsilon u_1 + \epsilon^2 u_2 + \dots \tag{13a}$$

$$v = v_0 + \epsilon v_1 + \epsilon^2 v_2 + \dots \tag{13b}$$

In the sequel, only the first two time scales T_0 and T_1 are retained. Substituting Eq. (13) and the time derivative rules into Eq. (12) and equating coefficients of same powers of ϵ, we obtain

$$\text{Order } \epsilon^0: \quad D_0^2 u_0 + u_0 = 0 \tag{14a}$$

$$D_0^2 v_0 + \mu D_0 v_0 - \beta v_0 + \alpha v_0^3 = 0. \tag{14b}$$

$$
\begin{aligned}
\text{Order } \epsilon^1: \quad & D_0^2 u_1 + u_1 = -\lambda u_0^2 D_0 u_0 + \sigma D_0 u_0 - 2 D_0 D_1 u_0 + u_0 - v_0 && \text{(15a)}\\
& D_0^2 v_1 + \mu D_0 v_1 - \beta v_1 + \alpha v_1^3 = \\
& \qquad - \mu D_1 v_0 - 2 D_0 D_1 v_0 + u_0 - u_1 + \alpha v_1^3 - 3\alpha v_0^2 v_1 . && \text{(15b)}
\end{aligned}
$$

The harmonic solution of Eq. (14a) is written on the following complex form

$$
u_0(T_0, T_1) = \frac{A(T_1) e^{iT_0} + A^*(T_1) e^{-iT_0}}{2} \tag{16}
$$

where A^* is the complex conjugate of the complex amplitude A.

Equation (14b) is the equation of motion of the BNES alone and has no analytical solution. Then the Harmonic Balance Method (HBM) is used to find an approximated solution as the following two-terms Fourier series

$$
v_0(T_0, T_1) = b_0(T_1) + \frac{C_0(T_1) e^{iT_0} + C_0^*(T_1) e^{-iT_0}}{2} \tag{17}
$$

where the first term in the right-hand side is real and used to take into account the bistable nature of the BNES, i.e., the fact that v_0 can have nonzero-mean. The second term indicates the simplification - due to the assumption of a 1:1 resonance capture - of the oscillating motion of v_0 as a simple harmonic motion.

Substituting Eq. (17) into Eq. (14b) and equalizing the coefficients of e^0 (mean terms) and e^{iT_0} (first harmonic terms) the following complex algebraic equations are obtained,

$$
-\beta b_0 + \frac{3}{2} \alpha C_0 |b_0|^2 + \alpha b_0^3 = 0 \tag{18a}
$$

$$
4\left(A + C_0\left(-\beta + 3\alpha b_0^2 + i\mu - 1\right)\right) + 3\alpha C_0 |C_0|^2 = 0, \tag{18b}
$$

respectively.

Let us now deal with Eq. (15). The first step is to substitute Eqs. (16) and (17) into Eq. (15a) and to eliminate secular terms. That leads to the following solvability condition

$$
D_1 A = \frac{1}{8}\left(4A(\sigma - i) + 4iC_0 - \lambda A |A|^2\right). \tag{19}
$$

The particular non-diverging solution of Eq. (15a) is then obtained, it is

$$
u_1(T_0, T_1) = -b_0(T_1) - \frac{1}{64} i\lambda \left(A(T_1)^3 e^{3iT_0} - A^*(T_1)^3 e^{-3iT_0}\right). \tag{20}
$$

The second step is to find $v_1(T_1, T_2)$ and again the HBM is used assuming the following form

$$
v_1(T_0, T_1) = b_1(T_1) + \frac{C_1(T_1) e^{iT_0} + C_1^*(T_1) e^{-iT_0}}{2}. \tag{21}
$$

Substituting Eqs. (16), (17), (20) and (21) into Eq. (15b) and again equating the coefficients of e^0 and e^{iT_0} the following differential equations are obtained

$$
D_1 b_0 = \frac{1}{2\mu}\Big(b_1\left(2\beta - 3\alpha C_0 \overline{C_0}\right) + b_0\left(2 - 3\alpha\left(C_0 \overline{C_1} + C_1 \overline{C_0}\right)\right) - 6\alpha b_1 b_0^2\Big), \tag{22}
$$

and

$$D_1C_0 = \frac{1}{4(\mu+2i)}\Big(2C_1\left(-3\alpha C_0\overline{C_0}+2\beta-6\alpha b_0^2-2i\mu+2\right)-3\alpha C_0\left(C_0\overline{C_1}+8b_0b_1\right)\Big), \tag{23}$$

respectively.

The MSM procedure is stopped at order ϵ^1. The last step of the MSHBM is then to come back to the physical time t. To achieve that we use the rules $b = b_0 + \epsilon b_1$ and $C = C_0 + \epsilon C_1$ and the fact that the variables A, B and C do not depend on the fast time T_0, therefore for them we have $\frac{d}{dt} = \epsilon D_1$. First, from Eq. (19) we obtain

$$\dot{A} = \frac{\epsilon}{8}\left(4A(\sigma-i)+4iC-\lambda A|A|^2\right). \tag{24}$$

Then combining Eq. (18a) with Eq. (22) and Eq. (18b) with Eq. (23) and keeping only terms of order equal to 1 or less in ϵ we have

$$\dot{b} = \frac{C\left(-3\alpha\left(|C|^2+4b^2\right)+4(\beta-i\mu+1)\right)-4b}{4(\mu+2i)}, \tag{25}$$

and

$$\dot{C} = \frac{b\left(2\beta-2\alpha b^2-3\alpha|C|^2\right)}{2\mu}+\epsilon\frac{b}{\mu}, \tag{26}$$

respectively.

Equations (24) to (26) constitute the complex form of the APMD. Finally, substituting A and C in the complex APMD by their polar coordinates defined as $A = ae^{j\theta}$ and $C = ce^{j\phi}$, new equations of motion for the real amplitudes a, b and c and the phase difference $\delta = \theta - \phi$ is obtained as

$$\dot{a} = \epsilon f(a,c,\delta) \tag{27a}$$

$$\dot{b} = g_1(b,c,\epsilon) \tag{27b}$$

$$\dot{c} = g_2(a,b,c,\delta) \tag{27c}$$

$$\dot{\delta} = g_3(a,b,c,\delta,\epsilon) \tag{27d}$$

with

$$f(a,c,\delta) = \frac{1}{8}\left(4a\sigma-a^3\lambda+4c\sin\delta\right) \tag{28a}$$

$$g_1(b,c,\epsilon) = \frac{b\left(2\beta-2\alpha b^2-3\alpha c^2\right)}{2\mu}+\epsilon\frac{b}{\mu} \tag{28b}$$

$$g_2(a,b,c,\delta) = -\frac{4a\mu\cos\delta+8a\sin\delta+c\mu\left(-4\beta+3\alpha\left(4b^2+c^2\right)+4\right)}{4\left(\mu^2+4\right)} \tag{28c}$$

$$\begin{aligned} g_3(a,b,c,\delta,\epsilon) = &-\frac{4a\cos\delta-2a\mu\sin\delta+3\alpha c\left(4b^2+c^2\right)-2c\left(2\beta+\mu^2+2\right)}{2c\left(\mu^2+4\right)}- \\ &\epsilon\frac{a-c\cos\delta}{2a}. \end{aligned} \tag{28d}$$

Equation (27) constitutes the real form of the APMD.

Due to the presence of the small parameter ϵ, the APMD is governed by two different time scales: the fast time scale t and the slow time scale $\tau = \epsilon t$ (note that t and τ were denoted above T_0 and T_1, respectively, in the context of the MSM). More precisely, within the framework of the geometric singular perturbation theory [29], Eq. (27) appears as a $(3, 1)$-fast-slow system where b, c and δ are the fast variables and a the slow variable. Periodic steady-state regimes of the original mechanical system (2) correspond to non trivial fixed points of the APMD whereas periodic responses of the latter characterize amplitude and phase modulated responses of the original dynamics.

4. Fast-slow analysis of the amplitude-phase modulation dynamics

4.1. The critical manifold

A key mathematical tool for the description of a fast-slow system such as Eq. (27) is its critical manifold. The latter is defined in this section. First, the APMD (27) is written with respect to the slow time τ as follows

$$a' = f(a, c, \delta) \tag{29a}$$
$$\epsilon b' = g_1(b, c, \epsilon) \tag{29b}$$
$$\epsilon c' = g_2(a, b, c, \delta) \tag{29c}$$
$$\epsilon \delta' = g_3(a, b, c, \delta, \epsilon) \tag{29d}$$

where $(.)'$ denotes the derivative with respect to the slow time τ. Considering $\epsilon = 0$ respectively in Eqs. (29) and (27) yields the *slow subsystem*

$$a' = f(a, c, \delta) \tag{30a}$$
$$0 = g_1(a, b, c, \delta, 0) \tag{30b}$$
$$0 = g_2(a, b, c, \delta) \tag{30c}$$
$$0 = g_3(a, b, c, \delta, 0) \tag{30d}$$

which is a differential-algebraic equation, and the *fast subsystem*

$$\dot{a} = 0 \tag{31a}$$
$$\dot{b} = g_1(a, b, c, \delta, 0) \tag{31b}$$
$$\dot{c} = g_2(a, b, c, \delta) \tag{31c}$$
$$\dot{\delta} = g_3(a, b, c, \delta, 0). \tag{31d}$$

The critical manifold of the APMD (27) is the solution of the algebraic part of the slow sub system (30) and it is expressed as follows

$$\mathcal{M}_0 = \Big\{ (a, b, c, \delta) \in \mathbb{R}^{+^3} \times [-\pi, \pi] \;\Big|\; g_1(b, c, 0) = 0 \;,\; g_2(a, b, c, \delta) = 0 \;\text{ and }\; g_3(a, b, c, \delta, 0) = 0 \Big\}. \tag{32}$$

The functions $g_1(b, c, 0) = 0$, $g_2(a, b, c, \delta) = 0$ and $g_3(a, b, c, \delta, 0) = 0$ are written as follows

$$g_1(a, b, c, \delta, 0) = b\,(b + H_{01}(c))\,(b - H_{01}(c)) \tag{33a}$$
$$g_2(a, b, c, \delta) = H_{02}(b, c) + a\,(k_1 \cos\delta + k_2 \sin\delta) \tag{33b}$$
$$g_3(a, b, c, \delta, 0) = H_{03}(b, c) + \frac{a}{c}\,(k_2 \cos\delta + k_1 \sin\delta)\,. \tag{33c}$$

where the function H_{01} is given below in Eq. (38b) and the functions H_{02} and H_{03} and the parameters k_1 and k_2 can be easily deduced from Eqs. (28c) and (28d).

The critical manifold can be expressed as a one-dimensional manifold evolving in the four-dimensional phase space of the APMD. Indeed, solving first Eqs. (30c) and (30d) yield

$$\begin{aligned}\cos\delta &= -\frac{k_1 H_{02}(b,c) + k_2 c H_{03}(b,c)}{a\left(k_1^2+k_2^2\right)}\\ &= -\frac{12\alpha b^2 c + 3\alpha c^3 - 4\beta c - 4c}{4a} \qquad (34)\\ \sin\delta &= -\frac{k_2 H_{02}(b,c) - k_1 c H_{03}(b,c)}{a\left(k_1^2+k_2^2\right)}\\ &= -\frac{c\mu}{a}. \qquad (35)\end{aligned}$$

Afterwards, combining Eqs. (34) and (35) with $a > 0$ leads to the following amplitude and phase equations

$$\begin{aligned}a &= \frac{\sqrt{c^2 H_{03}(b,c)^2 + H_{02}(b,c)^2}}{\sqrt{k_1^2+k_2^2}}\\ &= \frac{1}{4}c\sqrt{\left(3\alpha\left(4b^2+c^2\right) - 4(\beta+1)\right)^2 + 16\mu^2} \qquad (36)\\ \tan\delta &= \frac{k_2 H_{02}(b,c) - k_1 c H_{03}(b,c)}{k_1 H_{02}(b,c) + k_2 c H_{03}(b,c)}\\ &= \frac{4\mu}{3\alpha\left(4b^2+c^2\right) - 4(\beta+1)}. \qquad (37)\end{aligned}$$

Then solving Eq. (30b) we obtain the three possible expressions of b (which reflect the bistability of the BNES) as functions of c

$$b = 0 \qquad (38a)$$

$$b = \pm H_{01}(c) = \pm\sqrt{\frac{2\beta - 3\alpha c^2}{2\alpha}} \qquad (38b)$$

Equation (38b) shows that we must have $c < c^{\mathrm{I}}$, with

$$c^{\mathrm{I}} = \sqrt{\frac{2\beta}{3\alpha}}, \qquad (39)$$

for b to be real.

Finally, combining Eq. (36) with each of the equations of (38) we obtain the two amplitudes branches of $\mathcal{M}_0$ (only two because b appears squared in Eq. (36))

$$a = H_1(c) = \frac{1}{4}c\sqrt{\left(3\alpha c^2 - 4(\beta+1)\right)^2 + 16\mu^2} \qquad (40a)$$

$$a = H_2(c) = \frac{1}{4}c\sqrt{\left(-8\beta + 15\alpha c^2 + 4\right)^2 + 16\mu^2}. \qquad (40b)$$

In the same way, combining Eq. (37) with each of the equations of (38) we obtain

$$\sin\delta = G_1^{\mathrm{s}}(c) = -\mu\frac{c}{a}, \qquad \cos\delta = G_1^{\mathrm{c}}(c) = \frac{c\left(4\beta - 3\alpha c^2 + 4\right)}{4a}, \tag{41a}$$

$$\sin\delta = G_2^{\mathrm{s}}(c) = -\mu\frac{c}{a}, \qquad \cos\delta = G_2^{\mathrm{c}}(c) = \frac{c\left(-8\beta + 15\alpha c^2 + 4\right)}{4a}. \tag{41b}$$

The critical manifold can be therefore expressed as $\mathcal{M}_0 = \mathcal{M}_{01} \cup \mathcal{M}_{02}$ with

$$\mathcal{M}_{01} = \Big\{ (a,b,c,\delta) \in \mathbb{R}^{+^3} \times [-\pi,\pi] \ \Big| \ a = H_1(c)\ ,\ b = 0\ ,\ \sin\delta = G_1^{\mathrm{s}}(c)\ ,\ \cos\delta = G_1^{\mathrm{c}}(c) \Big\}, \tag{42a}$$

$$\mathcal{M}_{02} = \Big\{ (a,b,c,\delta) \in \mathbb{R}^{+^2} \times [0,\sqrt{\tfrac{2\beta}{3\alpha}}] \times [-\pi,\pi] \ \Big| \ a = H_2(c)\ ,\ b = H_{01}(c)\ ,\ \sin\delta = G_2^{\mathrm{s}}(c)\ ,\ \cos\delta = G_2^{\mathrm{c}}(c) \Big\}. \tag{42b}$$

Note that the two branches intersect when $H_{01}(c) = 0$, i.e., for $c = c^{\mathrm{I}}$ (see Eq. (39)).

Exploiting the polynomial properties of $H_1(c)$ and $H_2(c)$, the local extrema of these functions, i.e, the solutions of $\frac{dH_1}{dc} = 0$ and $\frac{dH_2}{dc} = 0$, respectively, can be computed. The local extrema of $H_1(c)$, denoted as c_1^{LF} and c_1^{RF}, are given by

$$c_1^{\mathrm{LF}} = \frac{2}{3}\sqrt{\frac{2\beta + 2 - \sqrt{(\beta+1)^2 - 3\mu^2}}{\alpha}} \tag{43a}$$

$$c_1^{\mathrm{RF}} = \frac{2}{3}\sqrt{\frac{2\beta + 2 + \sqrt{(\beta+1)^2 - 3\mu^2}}{\alpha}} \tag{43b}$$

if the following relation holds

$$\mu < \frac{\beta+1}{\sqrt{3}}. \tag{44}$$

If the condition (44) is not satisfied, the function $H_1(c)$ no longer has local extrema. In the rest of the paper, one considers that the condition (44) always holds. The superscripts $()^{\mathrm{LF}}$ and $()^{\mathrm{RF}}$ refer to *left fold point* and *right fold point*, respectively. Indeed, in the (a,b,c,δ)-space, the two points $p_1^{\mathrm{LF}} = (a_1^{\mathrm{LF}}, 0, c_1^{\mathrm{LF}}, \delta^{\mathrm{LF}})$ and $p_1^{\mathrm{RF}} = (a_1^{\mathrm{RF}}, 0, c_1^{\mathrm{RF}}, \delta_1^{\mathrm{RF}})$ (where a_1^{LF}, a_1^{RF}, δ_1^{LF} and δ_1^{RF} are obtained from c_1^{LF} and c_1^{RF} using Eqs. (40a) and (41a) and the b coordinate is null by Eq. (38a)) are generally called *fold points*.

Similarly, the local extrema of $H_2(c)$, denoted as c_2^{LF} and c_2^{RF}, are given by

$$c_2^{\mathrm{LF}} = \frac{2}{3}\sqrt{\frac{4\beta - 2 - \sqrt{(1-2\beta)^2 - 3\mu^2}}{5\alpha}} \tag{45a}$$

$$c_2^{\mathrm{RF}} = \frac{2}{3}\sqrt{\frac{4\beta - 2 + \sqrt{(1-2\beta)^2 - 3\mu^2}}{5\alpha}} \tag{45b}$$

if the following relations hold

$$\beta > \frac{1}{2} \tag{46}$$

and

$$\mu < \frac{2\beta - 1}{\sqrt{3}}. \tag{47}$$

If the conditions (46) and (47) are not satisfied, the function H_2 no longer has local extrema. Again, we will study cases where these conditions are always satisfied. As above, for the branch $\mathcal{M}_{01}$, one can define left and right fold points for the branch $\mathcal{M}_{02}$ as $p_2^{\mathrm{LF}} = (a_2^{\mathrm{LF}}, b_2^{\mathrm{LF}}, c_2^{\mathrm{LF}}, \delta^{\mathrm{LF}})$ and $p_2^{\mathrm{RF}} = (a_2^{\mathrm{RF}}, b_2^{\mathrm{RF}}, c_2^{\mathrm{RF}}, \delta_2^{\mathrm{RF}})$ (where a_2^{LF}, a_2^{RF}, b_2^{LF}, b_2^{RF}, δ_2^{LF} and δ_2^{RF} are obtained from c_2^{LF} and c_2^{RF} using Eqs. (38b), (40b) and (41b)).

Other important scalars for the present study, denoted as c_1^{D} and c_1^{U}, are obtained solving $H_1\left(c_1^{\mathrm{RF}}\right) = H_1\left(c_1^{\mathrm{D}}\right)$ and $H_1\left(c_1^{\mathrm{LF}}\right) = H_1\left(c_1^{\mathrm{U}}\right)$

$$c_1^{\mathrm{D}} = \frac{2}{3}\sqrt{\frac{2\beta + 2 - \sqrt[3]{\left((\beta+1)^2 - 3\mu^2\right)^{3/2}} - \frac{(\beta+1)^2 - 3\mu^2}{\sqrt[3]{\left((\beta+1)^2 - 3\mu^2\right)^{3/2}}}}{\alpha}} \tag{48a}$$

$$c_1^{\mathrm{U}} = \frac{2}{3}\sqrt{\frac{2\beta + 2 + \sqrt[3]{\left((\beta+1)^2 - 3\mu^2\right)^{3/2}} + \frac{(\beta+1)^2 - 3\mu^2}{\sqrt[3]{\left((\beta+1)^2 - 3\mu^2\right)^{3/2}}}}{\alpha}}. \tag{48b}$$

Similarly, if c_2^{RF} and c_2^{LF} exist, solving $H_2\left(c_2^{\mathrm{RF}}\right) = H_2\left(c_2^{\mathrm{D}}\right)$ and $H_2\left(c_2^{\mathrm{LF}}\right) = H_2\left(c_2^{\mathrm{U}}\right)$ yields

$$c_2^{\mathrm{D}} = \frac{2}{3}\sqrt{\frac{4\beta - 2 - \sqrt[3]{\left((1-2\beta)^2 - 3\mu^2\right)^{3/2}} - \frac{(1-2\beta)^2 - 3\mu^2}{\sqrt[3]{\left((1-2\beta)^2 - 3\mu^2\right)^{3/2}}}}{5\alpha}} \tag{49a}$$

$$c_2^{\mathrm{U}} = \frac{2}{3}\sqrt{\frac{4\beta - 2 + \sqrt[3]{\left((1-2\beta)^2 - 3\mu^2\right)^{3/2}} + \frac{\left(\left((1-2\beta)^2 - 3\mu^2\right)^{3/2}\right)^{2/3}}{\sqrt{(1-2\beta)^2 - 3\mu^2}}}{5\alpha}}. \tag{49b}$$

A typical example of the critical manifold in the (c, a)-plane is shown in Fig. 6(a). The fold points $(c_i^{\mathrm{LF}}, a_i^{\mathrm{LF}})$ and $(c_i^{\mathrm{RF}}, a_i^{\mathrm{RF}})$ $(i = 1, 2)$, the points $(c_i^{\mathrm{U}}, a_i^{\mathrm{LF}})$ and $(c_i^{\mathrm{D}}, a_i^{\mathrm{RF}})$ and the point $(c^{\mathrm{I}}, a^{\mathrm{I}})$ (with $a^{\mathrm{I}} = H_1(c^{\mathrm{I}}) = H_2(c^{\mathrm{I}})$, see Eq. (39)) are represented. Moreover, a zoom has been made to better see the shape of $\mathcal{M}_{01}$. The same example of the critical manifold in the (b, c, a)-space is shown in Fig. 6(b).

Because the conditions (44), (46) and (47) are satisfied, we can see that both $\mathcal{M}_{01}$ and $\mathcal{M}_{02}$ are S-shaped which suggests that several scenarios of relaxation oscillations are possible. To describe them (and other possible regimes), that requires knowing the stability of the critical manifold as well as the fixed points of the APMD. This is done in the next sections.

4.2. Stability analysis of the critical manifold

The stability of the critical manifold $\mathcal{M}_0$ is now investigated. For that, the Jacobian matrix $\mathbf{J_g}$ of Eqs. (31b) to (31d) is computed and evaluated at any point of each branch of the critical

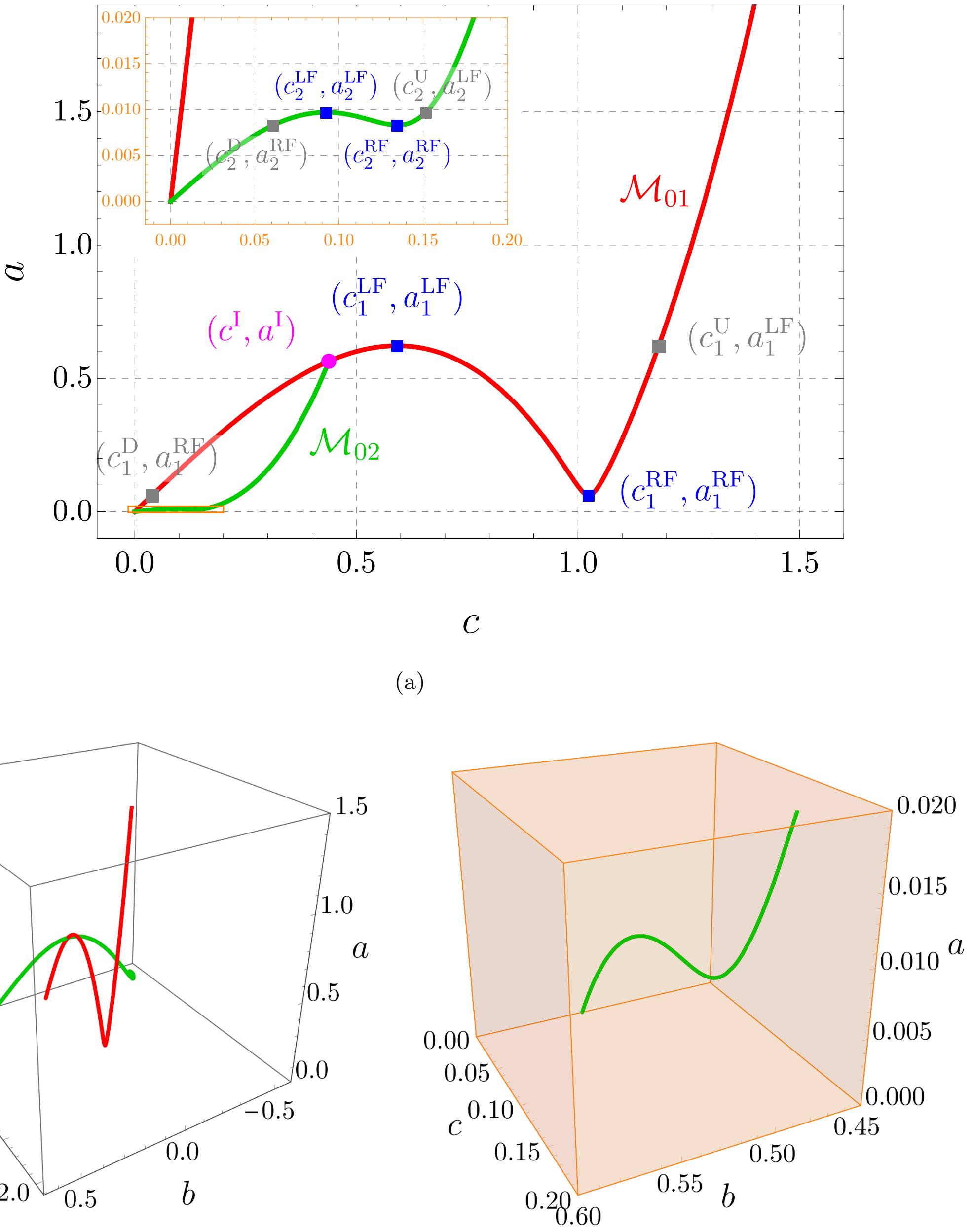

(a)

(b)

(c)

Figure 6: Typical example of the critical manifold. (a) In the (c, a)-plane. The branches $a = H_1(c)$ $(\mathcal{M}_{01})$ and $a = H_2(c)$ $(\mathcal{M}_{02})$ are plotted in red and green, respectively. The fold points $(c_i^{\mathrm{LF}}, a_i^{\mathrm{LF}})$ and $(c_i^{\mathrm{RF}}, a_i^{\mathrm{RF}})$ $(i = 1, 2)$ (blue points), the points $(c_i^{\mathrm{U}}, a_i^{\mathrm{LF}})$ and $(c_i^{\mathrm{D}}, a_i^{\mathrm{RF}})$ (gray points) and the point $(c^{\mathrm{I}}, a^{\mathrm{I}})$ (with $a^{\mathrm{I}} = H_1(c^{\mathrm{I}}) = H_2(c^{\mathrm{I}})$, see Eq. (39)) (magenta point) are also represented. A zoom is made to better see the shape of $\mathcal{M}_{01}$. (b) In the (b, c, a)-space. (c) Zoom of (b) corresponding to the orange colored rectangular cuboid area. The following parameters are used: $\mu = 0.1$, $\beta = 0.65$ and $\alpha = 2$.

manifold. We obtain

$$\mathbf{J}_{\mathbf{g}}(p_1) = \begin{pmatrix} -H_{01}(c)^2 & 0 & 0 \\ \dfrac{\partial H_{02}}{\partial b}(0, c) & \dfrac{\partial H_{02}}{\partial c}(0, c) & -cH_{03}(0, c) \\ \dfrac{\partial H_{03}}{\partial b}(0, c) & \dfrac{\partial H_{03}}{\partial c}(0, c) + \dfrac{H_{03}(0, c)}{c} & \dfrac{H_{02}(0, c)}{c} \end{pmatrix}, \tag{50}$$

for a point $p_1 \in \mathcal{M}_{01}$, and

$$\mathbf{J_g}(p_2) = \begin{pmatrix} 2H_{01}(c)^2 & -2H_{01}(c)^2 H_{01}'(c) & 0 \\ \dfrac{\partial H_{02}}{\partial b}(H_{01}(c), c) & \dfrac{\partial H_{02}}{\partial c}(H_{01}(c), c) & -cH_{03}(H_{01}(c), c) \\ \dfrac{\partial H_{03}}{\partial b}(H_{01}(c), c) & \dfrac{\partial H_{03}}{\partial c}(H_{01}(c), c) + \dfrac{H_{03}(H_{01}(c), c)}{c} & \dfrac{H_{02}(H_{01}(c), c)}{c} \end{pmatrix}, \tag{51}$$

for a point $p_2 \in \mathcal{M}_{02}$.

The critical manifold $\mathcal{M}_0$ contains both regular points defined as $\det(\mathbf{J_g}(p_i)) \neq 0$ $(i = 1, 2)$ and singular points characterized by $\det(\mathbf{J_g}(p_i)) = 0$. Depending on the eigenvalues of $\mathbf{J_g}(p_i)$, the set of regular points can be split into several parts (see definitions in Chap. 3 of [34]), including normally hyperbolic *attracting* parts (all the eigenvalues have strictly negative real parts), normally hyperbolic *repelling* parts (all the eigenvalues have strictly positive real parts), normally hyperbolic saddle type parts (neither attracting nor repelling) and non normally hyperbolic parts (at least one eigenvalue has a zero real part). Note that at singular points the critical manifold is also not normally hyperbolic. In previous definitions, *normally* means that each point of $\mathcal{M}_0$ must be hyperbolic only in the the direction normal (i.e., non tangent) to itself (see e.g. Definition 2.3.4 and the explanations below [34]).

It can be shown that

$$\det(\mathbf{J_g}(p_1)) = -H_{01}(c)^2 \frac{dH_1}{dc}(c) \frac{\sqrt{k_1^2 + k_2^2}\sqrt{c^2 H_{03}(0, c)^2 + H_{02}(0, c)^2}}{c} \tag{52}$$

and

$$\det(\mathbf{J_g}(p_2)) = H_{01}(c)^2 \frac{dH_2}{dc}(c) \frac{2\sqrt{k_1^2 + k_2^2}\sqrt{c^2 H_{03}(H_{01}(c), c)^2 + H_{02}(H_{01}(c), c)^2}}{c}. \tag{53}$$

From Eqs. (52) and (53) we can deduce that the singular points of the critical manifold are, if they exist, the left and right fold points $(c_i^{\mathrm{LF}}, a_i^{\mathrm{LF}})$ and $(c_i^{\mathrm{RF}}, a_i^{\mathrm{RF}})$ $(i = 1, 2)$ of each branch $\mathcal{M}_{0i}$ (the blue points in Fig. 6) and also the point of intersection $(c^{\mathrm{I}}, a^{\mathrm{I}})$ between these two branches (the magenta point in Fig. 6).

The three eigenvalues of $\mathbf{J_g}(p_1)$ (resp. $\mathbf{J_g}(p_2)$) are numerically computed; real and imaginary parts of these eigenvalues are plotted in Fig. 7(a) (resp. Fig. 7(b)). Comparing Figs. 6 and 7, we can see that the fold points and the point of intersection between the two branches of the critical manifold are actually points for which the latter is not normally hyperbolic. In addition, we can observe that the branch $\mathcal{M}_{02}$ loses its normal hyperbolicity at a regular point for $c \approx 0.33$ (see Fig. 7(b) top). Using the Routh-Hurwitz stability criterion and the Cardano's method, the analytical expression of this regular non normally hyperbolic fixed point of the branch $\mathcal{M}_{02}$ of the critical manifold can be obtained. The corresponding expression of c, denoted by c^{FP}, is

$$c^{\mathrm{FP}} = \sqrt{x_k} = \sqrt{2\sqrt{\frac{-p}{3}} \cos\left(\frac{1}{3} \arccos\left(\frac{3q}{2p}\sqrt{\frac{3}{-p}}\right) + \frac{2\pi}{3}\right) - \frac{b_2}{3b_1}}. \tag{54}$$

The definitions of p and q and details on the computation of c^{FP} are given in Appendix Appendix B. As previously, the other coordinates of the fixed point, i.e., b^{FP}, a^{FP} and δ^{I}, can be deduced from c^{FP} using Eqs. (38b), (40b) and (41b)), respectively.

The previous stability analysis is summarized in Fig. 8 in which each branch $\mathcal{M}_{01}$ and $\mathcal{M}_{02}$ of the critical manifold is decomposed as follows

$$\mathcal{M}_{01} = \mathcal{M}_{01}^{\mathrm{st},1} \cup p^{\mathrm{I}} \cup \mathcal{M}_{01}^{\mathrm{a},1} \cup p_1^{\mathrm{LF}} \cup \mathcal{M}_{01}^{\mathrm{st},2} \cup p_1^{\mathrm{RF}} \cup \mathcal{M}_{01}^{\mathrm{a},2} \tag{55}$$

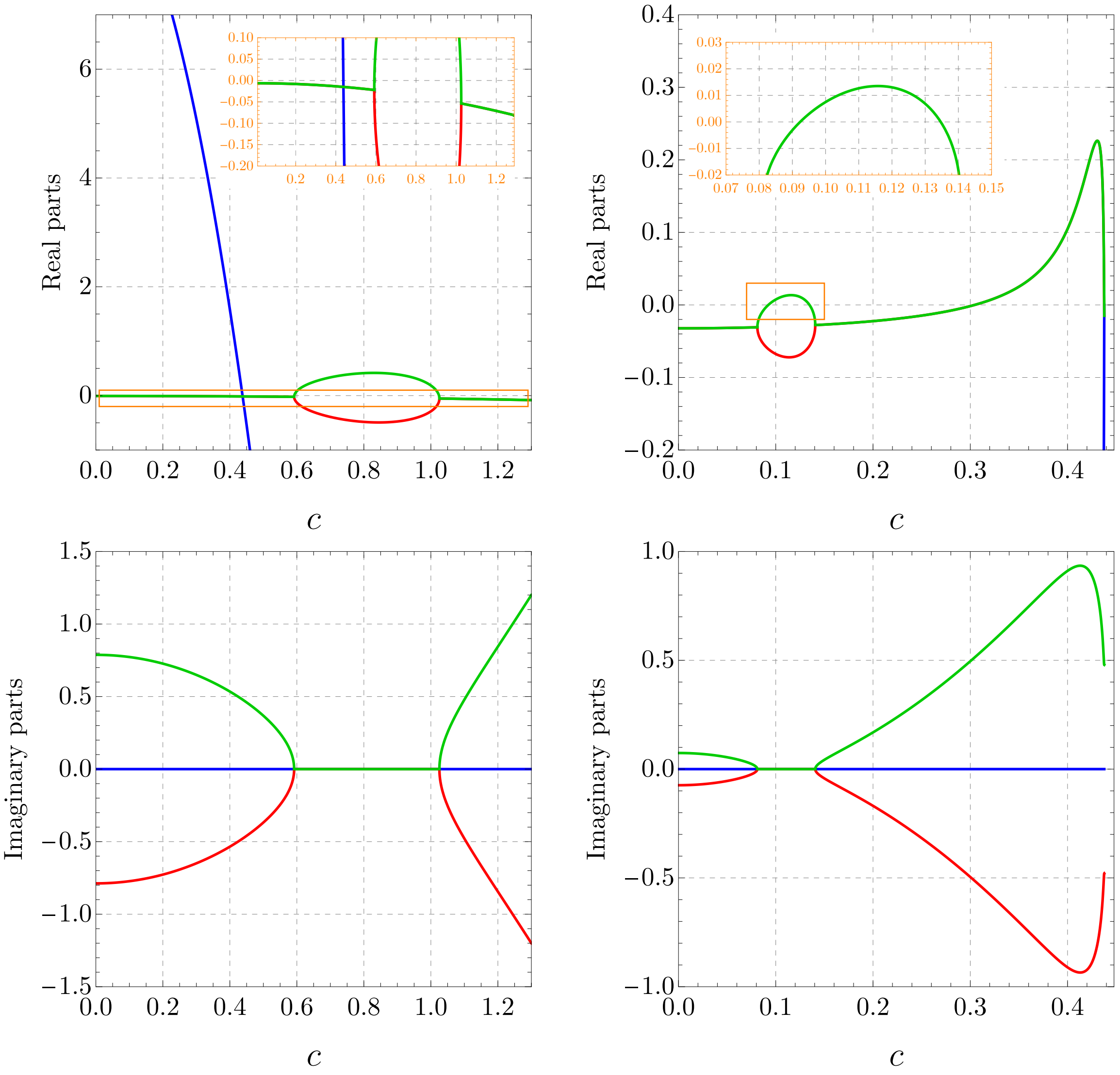

(a)

(b)

Figure 7: The three eigenvalues of (a) $\mathbf{J}_\mathbf{g}(p_1)$ given by (50) and (b) $\mathbf{J}_\mathbf{g}(p_2)$ given by (51). Top: real parts; Bottom: imaginary parts. The eigenvalues are numerically computed using the same BNES parameters as in Fig. 6.

with $p^{\mathrm{I}} = (a^{\mathrm{I}}, 0, c^{\mathrm{I}}, \delta^{\mathrm{I}})$ (where a^{I} and δ^{I} are obtained from c^{I} using Eqs. (40a) and (41a) and the b coordinate is null by Eq. (38a)), and

$$\mathcal{M}_{02} = \mathcal{M}_{02}^{\mathrm{a},1} \cup p_2^{\mathrm{LF}} \cup \mathcal{M}_{02}^{\mathrm{st},1} \cup p_1^{\mathrm{RF}} \cup \mathcal{M}_{01}^{\mathrm{a},2} \cup p^{\mathrm{FP}} \cup \mathcal{M}_{02}^{\mathrm{st},2} \cup p^{\mathrm{I}} \tag{56}$$

with $p^{\mathrm{FP}} = (a^{\mathrm{FP}}, b^{\mathrm{FP}}, c^{\mathrm{FP}}, \delta^{\mathrm{FP}})$ (where a^{FP}, b^{FP} and δ^{FP} are obtained from a^{I} using Eqs. (38b), (40b) and (41b)). In both previous expressions the superscripts “st” and “a” indicate the saddle-type and attracting natures of the critical manifold, respectively.

The structure of $\mathcal{M}_{02}$ can be modified if (46) or (47) does not hold, in this case $\mathcal{M}_{02}$ is not S-shaped anymore and $\mathcal{M}_{02}^{\mathrm{st},1}$ disappears. Moreover, if p^{FP} joins p^{I}, the branch $\mathcal{M}_{02}^{\mathrm{st},2}$ disappears.

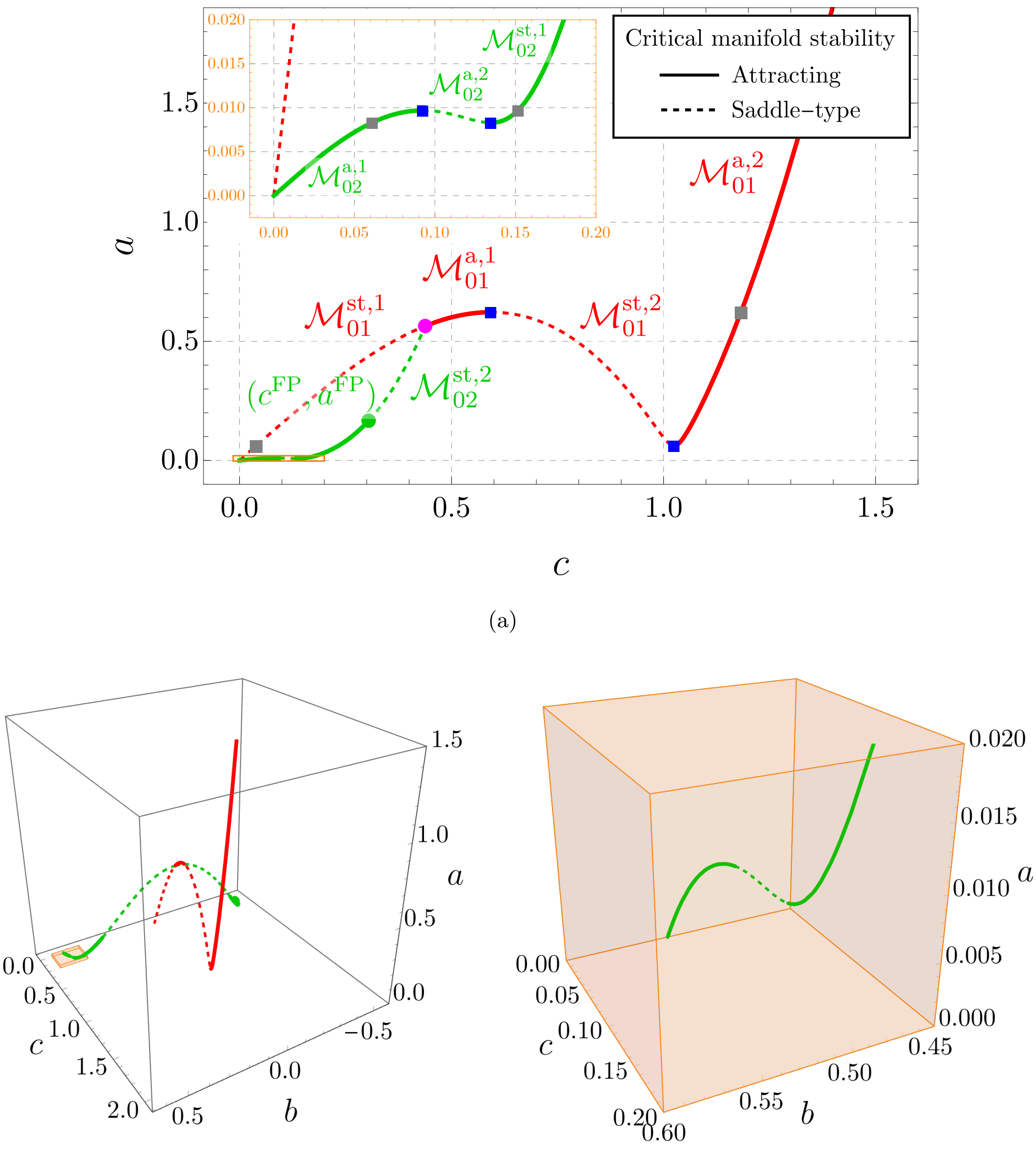

(a)

(b)

(c)

Figure 8: The different parts of the critical manifold $\mathcal{M}_0$. (a) In the (c, a)-plane. For the branch $\mathcal{M}_{01}$ (in red) one has (see Eq. (55)) from left to right: the first saddle-type branch $\mathcal{M}_{01}^{\mathrm{st},1}$, the first attracting branch $\mathcal{M}_{01}^{\mathrm{a},1}$, the second saddle-type branch $\mathcal{M}_{01}^{\mathrm{st},2}$ and the second attracting branch $\mathcal{M}_{01}^{\mathrm{a},2}$. These branches are respectively connected to each other by the point p^{I} (magenta point) and the left and right fold points p_1^{LF} and p_1^{RF} (blue points). For the branch $\mathcal{M}_{02}$ (in green) one has (see Eq. (56)) from left to right: the first attracting branch $\mathcal{M}_{02}^{\mathrm{a},1}$, the first saddle-type branch $\mathcal{M}_{02}^{\mathrm{st},1}$, the second attracting branch $\mathcal{M}_{02}^{\mathrm{a},2}$ and the second saddle-type branch $\mathcal{M}_{02}^{\mathrm{a},2}$ which ends at the point p^{I} . These branches are respectively connected to each other by the left and right fold points p_2^{LF} and p_2^{RF} (blue points) and the point p^{FP} (green point). (b) In the (b, c, a)-space. (c) Zoom of (b) corresponding to the orange colored rectangular cuboid area.

From the previous analysis, we can already give a partial description of the APMD behavior. In phase space, if the trajectory is not in the vicinity of the critical manifold, it evolves fast to an attracting part of the critical manifold. These fast epochs are approximately described by the fast subsystem (31). Bistability has been observed since several points of the critical manifold can be stable for a given set of parameters and a given value of the slow variable a (which, due to (31a), is a parameter for the fast subsystem). In the present paper the basins of attraction of each attracting branch of the critical manifold are not rigorously investigated, together with the possible other kinds of solutions of the fast subsystem (such as periodic, quasiperiodic or even chaotic motions). This can be investigated in the future.

In the vicinity of the critical manifold, the trajectory evolves slowly. These slow epochs are approximately described by the slow subsystem (30), its analysis is performed in the next section.

4.3. Asymptotic analytical expression of the fixed points of the amplitude-phase modulation dynamics

As mentioned previously, the fixed points of the APMD (29) (or (27)) characterize periodic solutions of the original system (2). Since $0 < \epsilon \ll 1$, these fixed points can be asymptotically approximated by those of the slow subsystem (30). Moreover, to obtain a simple analytical expression of these fixed points, it is first necessary to linearize the function f (see Eq. (28a)) around $a = 0$.

Then, using successively Eqs. (38a), (40a) and (41a) and Eqs.(38b), (40b) and (41b) the slow dynamics (30) on the branches $\mathcal{M}_{01}$ and $\mathcal{M}_{02}$ can be considered only with respect to c as

$$\frac{dH_1}{dc}(c)c' = F_1(c) \tag{57}$$

and

$$\frac{dH_2}{dc}(c)c' = F_2(c), \tag{58}$$

respectively. The expressions of the functions F_1 and F_2 in the previous equations are

$$F_1 = \frac{c\left(\sigma\left(3\alpha c^2 - 4(\beta+1)\right)^2 + 16\mu(\mu\sigma - 1)\right)}{8\sqrt{\left(3\alpha c^2 - 4(\beta+1)\right)^2 + 16\mu^2}}, \tag{59a}$$

$$F_2 = \frac{c\left(\sigma\left(-8\beta + 15\alpha c^2 + 4\right)^2 + 16\mu(\mu\sigma - 1)\right)}{8\sqrt{\left(-8\beta + 15\alpha c^2 + 4\right)^2 + 16\mu^2}}. \tag{59b}$$

Consequently, the desired fixed points are solutions of $F_1(c) = 0$ and $F_2(c) = 0$ of which $c = 0$ is a trivial solution. In the (b, c, a)-space, on $\mathcal{M}_{01}$ this gives $(0, 0, 0)$ which correspond to p_0^{st} (see Eq. (3)). On $\mathcal{M}_{02}$ that yields $(0, \pm\sqrt{\frac{\beta}{\alpha}}, 0)$ (see Eq. (38b)) which correspond to p_1^{st} and p_2^{st} (see Eq. (4)).

Then the non trivial solutions of $F_1(c) = 0$ and $F_2(c) = 0$ are computed. The terms in parentheses in the numerator of F_1 and F_2 are quadratic polynomials with respect to c^2. The corresponding positive solutions in terms of the variable c are

$$c^*_{1,1} = \sqrt{\frac{1+\beta-\sqrt{\mu\left(\frac{1}{\sigma}-\mu\right)}}{3\alpha}} \tag{60a}$$

$$c^*_{1,2} = \sqrt{\frac{1+\beta+\sqrt{\mu\left(\frac{1}{\sigma}-\mu\right)}}{3\alpha}} \tag{60b}$$

obtained solving $F_1(c) = 0$, and

$$c^*_{2,1} = 2\sqrt{\frac{2\beta-1-\sqrt{\mu\left(\frac{1}{\sigma}-\mu\right)}}{15\alpha}} \tag{61a}$$

$$c^*_{2,2} = 2\sqrt{\frac{2\beta-1+\sqrt{\mu\left(\frac{1}{\sigma}-\mu\right)}}{15\alpha}} \tag{61b}$$

obtained solving $F_2(c) = 0$.

One can easily verify from Eqs. (60) and (61) that $c^*_{2,1} < c^*_{2,2} < c^*_{1,1} < c^*_{1,2}$ and that these fixed points no longer exist when they become complex for

$$\sigma > \sigma^{\mathrm{S}} = \frac{1}{\mu}. \tag{62}$$

Other sets of parameters can make the above expressions complex, except $c^*_{1,2}$ which is always real if Eq. (62) holds.

Finally, the stability of the fixed points $c^*_{1,i}$ and $c^*_{2,i}$ $(i = 1, 2)$ is obtained checking the sign of $\frac{d}{dc}\left(\frac{F_1(c)}{\frac{dH_1}{dc}(c)}\right)\Big|_{c=c^*_{1,i}}$ and $\frac{d}{dc}\left(\frac{F_2(c)}{\frac{dH_2}{dc}(c)}\right)\Big|_{c=c^*_{2,i}}$ $(i = 1, 2)$, respectively.

The analysis presented in this section provides an approximate description of the slow dynamics of the APMD in the vicinity of an attracting branch of the critical manifold. However, slow dynamics around families of periodic, quasiperiodic or chaotic solutions of the fast subsystem is not investigated. Studies inspired from the work of Berglund and Gentz [35] on invariant manifold tracking the family of periodic orbits could be again the subject of future works.

5. Asymptotic global stability analysis of the amplitude-phase modulation dynamics

Knowing the fixed points of the APMD and their stability, obtained in Section 4.3, together with the analysis of the critical manifold presented in Section 4.2, allow to perform the global stability analysis of the APMD, again asymptotically in the case of $\epsilon \to 0$. This will enable us to interpret the observations made in Fig. 4. The analysis is possible analytically because the critical manifold is one-dimensional. Therefore the slow dynamics is also one-dimensional and described by Eqs. (57) and (58).

From Eqs. (11), (16), (17), (20), (21) and the rules $b = b_0 + \epsilon b_1$ and $C = C_0 + \epsilon C_1$, one has

$$y(t) = -\frac{b(t)\epsilon + b(t) - a(t)\cos(\theta(t)+t) + c(t)\cos(t+\varphi(t)) + \frac{1}{32}a(t)^3\lambda\epsilon\sin(3(\theta(t)+t))}{\epsilon+1}. \tag{63}$$

For comparison purposes, the time series $y(t)$ reconstructed from numerical simulations of the APMD using Eq. (63) are shown in Fig. 9. In Figs. 9(a) to 9(e) the parameters used are the same as in Figs. 4(a) to Figs. 4(e). We can see that the APMD can reproduce regimes of the same nature as those obtained with the full order system (2). In Figs. 9(f) and 9(g), even if the APMD can reproduce these two chaotic regimes, they are here obtained for smaller values of the bifurcation parameter of σ, namely $\sigma = 1.22$ and 0.77 for Figs. 9(f) and 9(g), respectively. In general when chaotic regimes occur the mitigation limit observed on the numerical simulation of the APMD is smaller than that obtained with the full order system (2).

To explain the nature of the different regimes shown in Figs. 4 and 9, the trajectories of the APMD in the (c, a)-plane (obtained from the same simulations as in Fig. 9) are superimposed on the critical manifold given by Eq. (40) in Fig. 10. The structure of the critical manifold (i.e, stability, fold points $(c_i^{\mathrm{LF}}, a_i^{\mathrm{LF}})$ and $(c_i^{\mathrm{RF}}, a_i^{\mathrm{RF}})$ $(i = 1, 2)$, points $(c_i^{\mathrm{U}}, a_i^{\mathrm{LF}})$ and $(c_i^{\mathrm{D}}, a_i^{\mathrm{RF}})$ and the point $(c^{\mathrm{I}}, a^{\mathrm{I}})$) is depicted in the same way as in Figs. 6 and 8. Fig. 10 shows also the fixed points of the APMD obtained in Section 4.3, i.e. the trivial fixed points[4] and the non trivial fixed points $(c_{1,i}^*, H_1(c_{1,i}^*))$ (in black color) and $(c_{2,i}^*, H_2(c_{2,i}^*))$ (in orange color) with $i = 1, 2$ and $c_{1,i}^*$ and $c_{2,i}^*$ given by Eqs. (61) and (61), respectively. These fixed points are depicted by a $\star$ when they are stable and a $\bullet$ when they are unstable.

The different regimes can now be explained as follows:

Fig. 10(a). The trivial fixed point on $\mathcal{M}_{02}^{\mathrm{a},1}$ is stable (depicted by an orange $\star$). The other fixed points on $\mathcal{M}_{02}^{\mathrm{a},1}$ is unstable (depicted by an orange $\bullet$). As long as the initial condition causes the APMD trajectory to arrive (after a fast epoch) on $\mathcal{M}_{02}^{\mathrm{a},1}$ between the unstable fixed point and the stable fixed point, the latter is reached after a slow epoch along $\mathcal{M}_{02}^{\mathrm{a},1}$, as in Fig. 10(a). The initial condition in the zoom (orange frame in Fig. 10(a)) is depicted by a blue $\bullet$.

Fig. 10(b). There is only the unstable trivial fixed point on $\mathcal{M}_{02}^{\mathrm{a},1}$ (for this set of parameters one has $\mathcal{M}_{02} = \mathcal{M}_{02}^{\mathrm{a},1}$). The trajectory follows slowly $\mathcal{M}_{02}^{\mathrm{a},1}$ until it disappears at $(c^{\mathrm{I}}, a^{\mathrm{I}})$ and then follows $\mathcal{M}_{01}^{\mathrm{a},1}$, slowly again. Finally, the trajectory stops on a stable fixed point (depicted by a black $\star$). Because on $\mathcal{M}_{01}$ $b = 0$ (see Fig. 8(b)), this scenario of the APMD explains the periodic regime PR1 observed in Fig. 4(b).

Fig. 10(c). The fixed point on $\mathcal{M}_{01}^{\mathrm{a},1}$ moves to the saddle-type part $\mathcal{M}_{01}^{\mathrm{st},2}$. Consequently, the trajectory evolves slowly to the left fold point $(c_1^{\mathrm{LF}}, a_1^{\mathrm{LF}})$ and undergoes a fast jump to $\mathcal{M}_{01}^{\mathrm{a},2}$. Because the unstable point on $\mathcal{M}_{01}^{\mathrm{a},2}$ (the black $\bullet$) is above $(c_i^{\mathrm{U}}, a_i^{\mathrm{LF}})$ (the gray $\blacksquare$) we then observe a succession of slow evolutions near the attracting branch of $\mathcal{M}_{01}$ and fast jumps (from $(c_1^{\mathrm{LF}}, a_1^{\mathrm{LF}})$ to $(c_i^{\mathrm{U}}, a_i^{\mathrm{LF}})$ and from $(c_1^{\mathrm{RF}}, a_1^{\mathrm{RF}})$ to $(c_i^{\mathrm{D}}, a_i^{\mathrm{RF}})$). These so-called *relaxation oscillations* on $\mathcal{M}_{01}$ explain the SMR1 observed in Fig. 4(c).

Fig. 10(d). There is a stable non trivial fixed point on $\mathcal{M}_{02}^{\mathrm{a},1}$ (the orange $\star$). The trivial fixed point and the other non trivial fixed point on $\mathcal{M}_{02}^{\mathrm{a},1}$ are unstable (the two orange $\bullet$). As long as the initial condition causes the APMD trajectory to arrive on $\mathcal{M}_{02}^{\mathrm{a},1}$ below the unstable non trivial fixed point, the stable fixed point is reached after a slow epoch along $\mathcal{M}_{02}^{\mathrm{a},1}$, as in Fig. 10(c). This scenario for the APMD corresponds to the periodic intra-well motion PR1 observed in Fig. 4(d).

---

[4] Remember that they correspond to p_0^{st} when they are on $\mathcal{M}_{01}$ and to p_1^{st} (or p_2^{st}) when they are on $\mathcal{M}_{02}$. They are superimposed in the (c, a)-plane but not in the (b, c, a)-space (see Section 4.3).

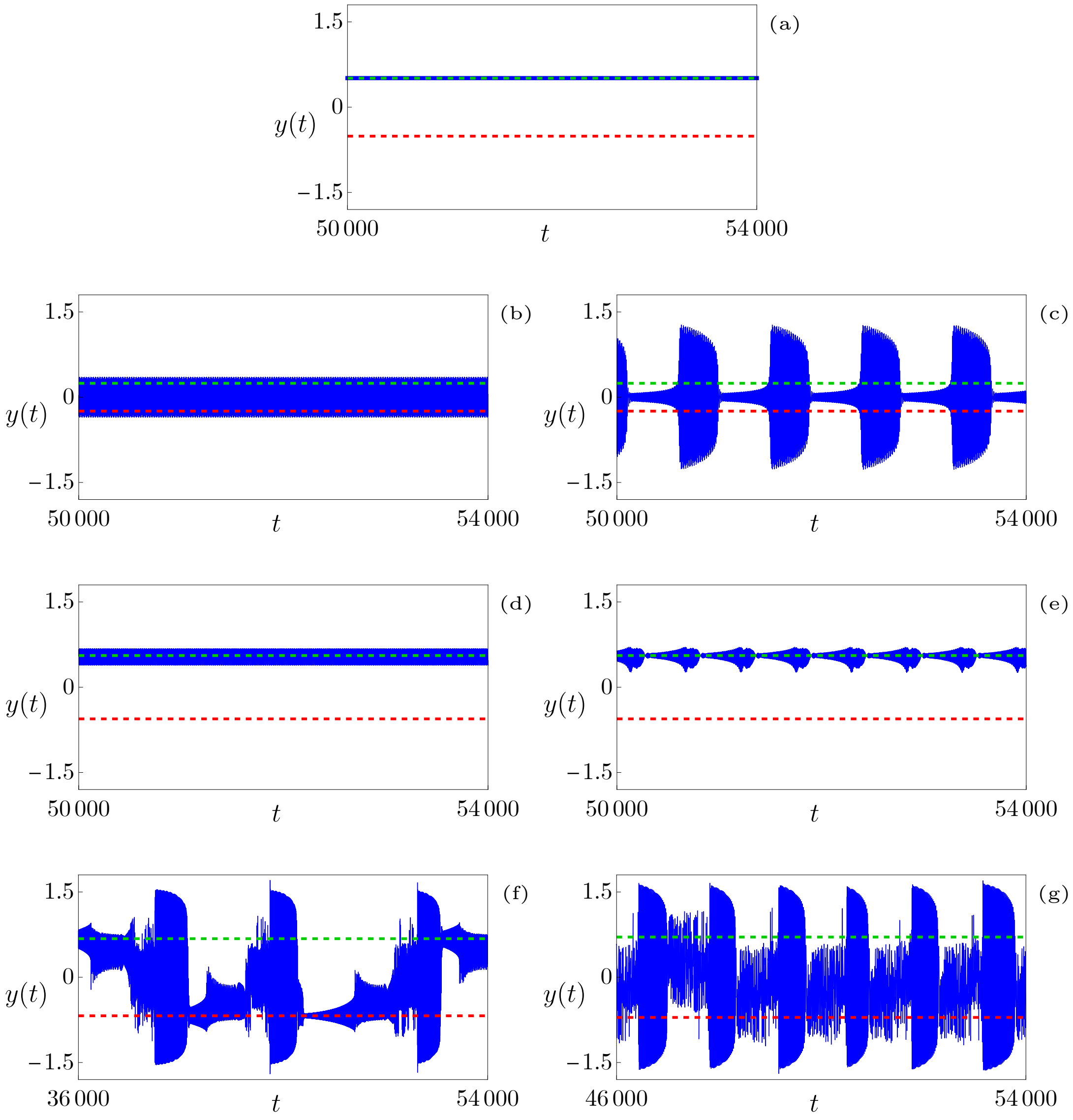

Figure 9: Time series $y(t)$ reconstructed from numerical simulations of the APMD using Eq. (63). Equilibrium positions y_1^{st} (dashed green line) and y_2^{st} (dashed blue line). From (a) to (e) the parameters used are the same as in Figs. 4(a) to Figs. 4(e). In (f) and (g) the value of σ is changed compared to Figs. 4(f) and 4(g), namely $\sigma = 1.22$ and 0.77, respectively.

Fig. 10(e). A scenario of relaxation oscillations on $\mathcal{M}_{02}$ (similar to that observed on $\mathcal{M}_{01}$ in Fig. 10(c)) is observed in agreement with the intra-well SMR2 of Fig. 4(d). Again, as long as the initial condition causes the APMD trajectory to arrive on $\mathcal{M}_{02}^{\mathrm{a},2}$ below the unstable non trivial fixed point, these relaxation oscillations will occur.

Fig. 10(f). For the sake of readability of the figure, only steady state motion is shown. This scenario is also illustrated in Fig. 11(a), showing the time series of the variables $b(t)$, $c(t)$ and $y(t)$ (computed again using Eq. (63)), and in Fig. 12(a) depicting the trajectory of the APMD in the (b, c, a)-space. For this scenario and the next one, when we speak of an equilibrium (resp. a periodic) regime during a slow epoch of the APMD, this means that for the set of parameters and the value of a considered, the fast subsystem has a stable equilibrium (resp. periodic) solution. The APMD therefore follows an invariant manifold tracking these equilibrium (resp. periodic) solutions and parameterized by the slow variable a. For full order dynamics (referred to as FOD in Fig. 11(a)), which includes oscillations at the natural frequency of the VdP oscillator, that corresponds to invariant manifold tracking of periodic (resp. quasiperiodic solutions). Chaotic motions are also encountered. The successive phases of the motion are described in Fig. 11(a). During a complete cycle, the trajectory of the APMD: follows $\mathcal{M}_{02}^{\mathrm{a},1}$ (SE1: APMD, equilibrium 1; FOD, periodic 1); undergoes a fast jump (FE2) from $(c_2^{\mathrm{LF}}, a_2^{\mathrm{LF}})$ and the corresponding left branch of $\mathcal{M}_{02}$ is saddle-type (i.e., $\mathcal{M}_{02}^{\mathrm{st},2}$); is periodic (quasiperiodic for the FOD) precisely because $\mathcal{M}_{02}$ is saddle-type and then chaotic (SE2); undergoes a fast jump (FE3) to $\mathcal{M}_{01}^{\mathrm{a},2}$; follows $\mathcal{M}_{01}^{\mathrm{a},2}$ (SE3: APMD, equilibrium 2; FOD, periodic 2); finally undergoes a fast jump (FE1') from $(c_1^{\mathrm{RF}}, a_1^{\mathrm{RF}})$ to $\mathcal{M}_{02}^{\mathrm{a},1}$; and so on. At each cycle there is the possibility of reaching one or other of the opposite $\mathcal{M}_{02}$ branches (see Fif. 12(a)). Concerning the start of the chaotic phases, we do not know whether this is really a chaotic movement of the fast subsystem or a quasi-periodic solution. Again, this may be subject of future work. This scenario of the APMD is in agreement with what we observed in Fig. 5(a) except that the Periodic 1 and Quasiperiodic 1 phases (for the FOD) appear to be reversed.

Fig. 10(g). Again, only steady state motion is shown and the scenario is also illustrated in Fig. 11(b), showing the time series of the variables $b(t)$, $c(t)$ and $y(t)$ (computed again using Eq. (63)), and in Fig. 12(b) depicting the trajectory of the APMD in the (b, c, a)-space. The successive phases of the motion are described in Fig. 11(b). When we observe the APMD, we see a periodic and then a chaotic regime during phases 1 and 1'. It is difficult to differentiate between these two phases on the $y(t)$ signal from the FOD. However, the latter is qualitatively equivalent to what we observed in Fig. 5(b).

In each of the previous situations we can see that if there is a passage on $\mathcal{M}_{01}$, it is the largest unstable fixed point (black • on $\mathcal{M}_{02}^{\mathrm{a},1}$) which prevents the system from tipping over into a harmful situation. If the trajectory ends up on $\mathcal{M}_{02}^{\mathrm{a},1}$, above this fixed point, it runs along $\mathcal{M}_{02}^{\mathrm{a},1}$ towards infinity (i.e. harmful situation) when the linearized VdP is considered (see Section 4.3). If the nonlinear VdP is considered, the trajectory reaches a stable fixed point with large amplitude similar to that of the VdP alone (i.e. also harmful situation).

Of course, the global stability analysis presented here is only partial. In the future, it will be necessary to rigorously research the possible solutions of the fast subsystem, as well as their stability. It will then be necessary to find the invariant manifolds of the APMD tracking these solutions. However, this study enables us to interpret a certain number of regimes observed on numerical simulations.

6. Conclusion

In this paper a Van der Pol oscillator (used as an archetypal self-sustained oscillator) coupled to a bistable nonlinear energy sink BNES) has been studied. Numerical simulations have shown that this system can undergo a multitude of motions including different types of periodic regimes and so-called strongly modulated responses (SMR) as well as chaotic regimes. We also show that a BNES can be much more efficient than a classical cubic NES but this is not robust since a little perturbation can switch the system from harmless to harmful situations. However, even in the most unfavorable cases, we were able to find a set of parameters for which the BNES performs better than the NES.

Then, in an original way, the so-called Multiple Scale/Harmonic Balance Method (MSHBM) is used and modified (compared to its usual use) to consider the specific feature of the BNES, i.e., that it can have a nonzero-mean oscillating motion. This allowed us to derive an amplitude-phase modulation dynamics (APMD) which can reproduce the complex behavior of the initial system.

Because of the presence of a small perturbation parameter (i.e., the mass ratio between the BNES and the VdP oscillator), the APMD is governed by two different time scales. More precisely, in its real form it appears as a (3,1)-fast-slow system. The motion of such a fast-slow system consists in a succession of slow and fast epochs. In the case of a classic cubic NES, the APMD is a (2,1)-fast-slow system whose behavior is now well understood. For example, the most complex responses are relaxation oscillations leading to so-called strongly modulated responses (SMR) for the initial system. Here, due to its (3,1)-fast-slow nature, the APMD can undergo a multitude of different motions including periodic and quasiperiodic regimes of different types and even chaotic regimes, in agreement with what has been observed on numerical simulations of the initial system. The fast-slow analysis of the APMD has been conducted within the framework of the geometric singular perturbation theory. By the computation of the so-called critical manifold and the analytical expressions of the APMD fixed points, a global stability analysis has been performed. This enabled us to interpret a certain number of regimes observed on numerical simulations of the initial system.

The methodology proposed here is applied to the study of passive mitigation of self-sustained oscillations using a BNES. Because of its general nature, it could be used in the future to study passive attenuation of free and forced vibrations. It could also be generalized to the case of a multistable NES.

Appendix A. Approximate analytical solution of the Van der Pol oscillator

The equation of motion of the VdP oscillator alone is

$$\ddot{x} + \epsilon h(x, \dot{x}) + x = 0. \tag{A.1}$$

with $h(x, \dot{x}) = -\sigma \dot{x} + \lambda \dot{x} x^2$.

An approximate analytical solution of Eq. (A.1) is found using the Krylov-Bogoliubov method of averaging (see e.g. [31]). For that, an amplitude phase representation of the motion is first introduced as

$$x = r(t)\cos\left(t + \varphi(t)\right) \tag{A.2a}$$

$$\dot{x} = -r(t)\sin\left(t + \varphi(t)\right) \tag{A.2b}$$

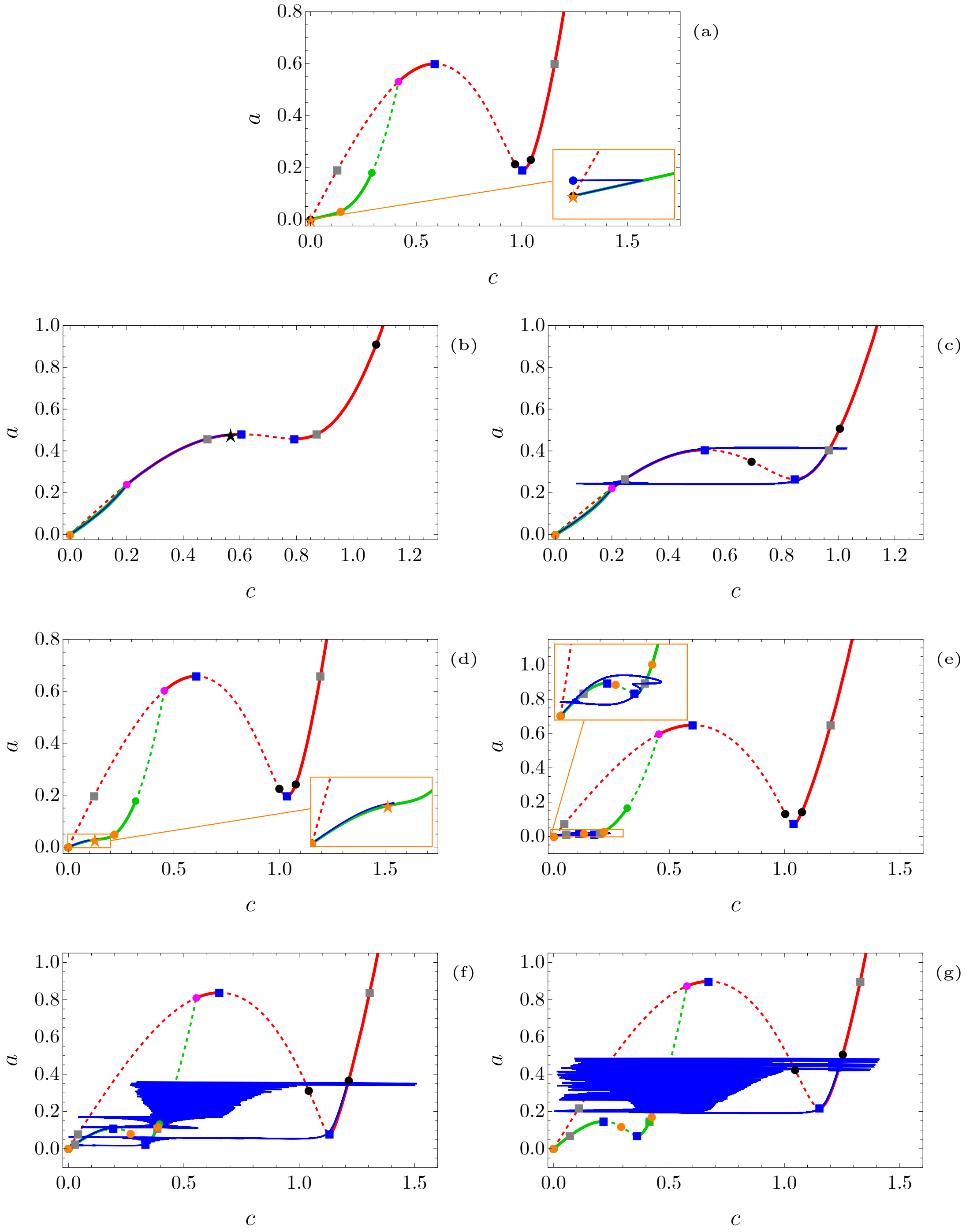

Figure 10: Trajectories of the APMD in the (c, a)-plane (obtained from the same simulations as in Fig. 9) are superimposed on the critical manifold given by Eq. (40). The structure of the critical manifold (i.e, stability, fold points $(c_i^{\mathrm{LF}}, a_i^{\mathrm{LF}})$ and $(c_i^{\mathrm{RF}}, a_i^{\mathrm{RF}})$ $(i = 1, 2)$, points $(c_i^{\mathrm{U}}, a_i^{\mathrm{LF}})$ and $(c_i^{\mathrm{D}}, a_i^{\mathrm{RF}})$ and the point $(c^{\mathrm{I}}, a^{\mathrm{I}})$) is depicted in the same way as in Figs. 6 and 8. Fixed points of the APMD obtained in Section 4.3, i.e. the trivial fixed points and the non trivial fixed points $(c_{1,i}^*, H_1(c_{1,i}^*))$ (in black color) and $(c_{2,i}^*, H_2(c_{2,i}^*))$ (in orange color) with $i = 1, 2$ and $c_{1,i}^*$ and $c_{2,i}^*$ given by Eqs. (61) and (61), respectively. These fixed points are depicted by a $\star$ when they are stable and a $\bullet$ when they are unstable.

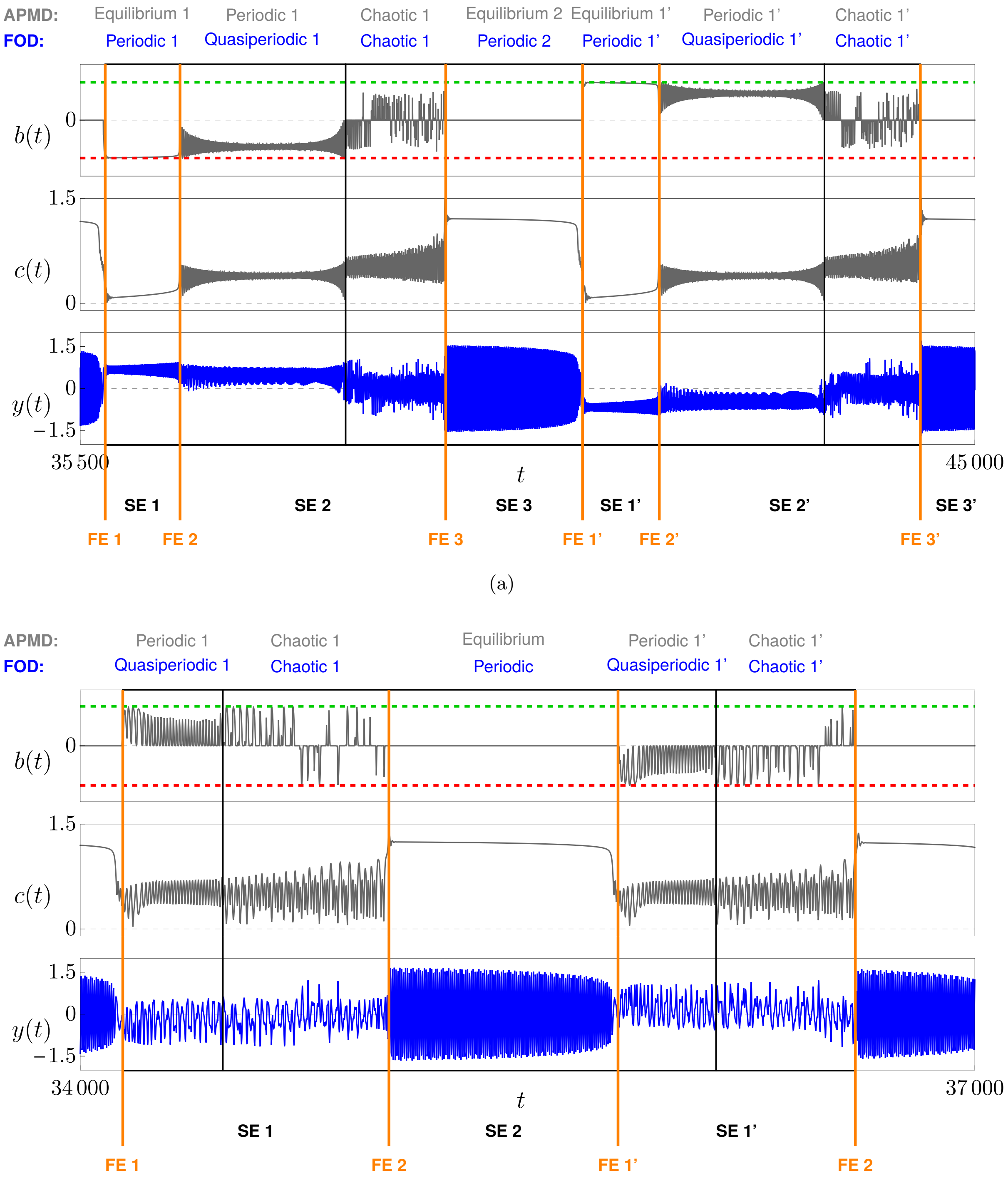

(a)

(b)

Figure 11: Same numerical simulations as in (a) Figs. 9(f) and (b) 9(g). For both (a) and (b) from top to bottom one has the time series $b(t)$ (gray), (c) (gray) and $y(t)$ (blue). The equilibrium positions $y_1^{\rm st}$ (dashed green line) and $y_2^{\rm st}$ (dashed blue line) are depicted in the plot of $b(t)$. One has APMD for amplitude-phase modulation dynamics, FOD for full order dynamics, FE for fast epoch and SE for slow epoch.

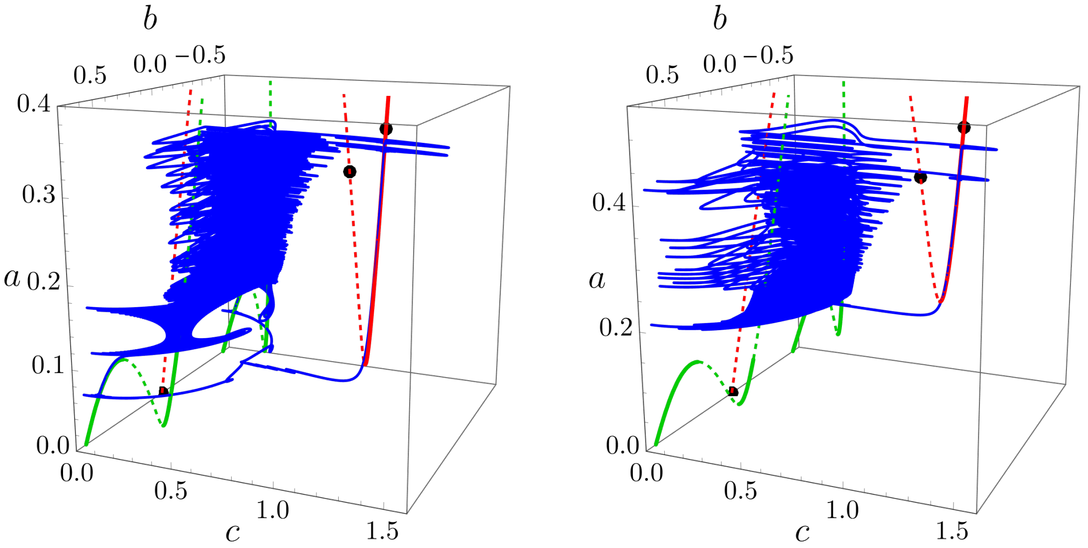

(a) (b)

Figure 12: Same numerical simulations as in (a) Figs. 9(f) and (b) 9(g) depicting the trajectory of the AMPD (blue) superimposed on the critical manifold $\mathcal{M}_{01}$ (attracting: red solid line; saddle-type: red dashed line) and $\mathcal{M}_{02}$ (attracting: green solid line; saddle-type: green dashed line). Unstable fixed points of the AMPD on $\mathcal{M}_{01}$ are also represented by black •.

The desired form of Eq. (A.2) requires that

$$\dot{r}\cos\gamma - r\dot{\varphi}\sin\gamma = 0, \tag{A.3}$$

with $\gamma = t + \varphi$ which yields

$$\dot{\varphi} = \frac{\dot{r}}{r}\frac{\cos\gamma}{\sin\gamma} \quad \text{and} \quad \dot{r} = r\dot{\varphi}\frac{\sin\gamma}{\cos\gamma}. \tag{A.4}$$

The time derivative of Eq. (A.2) is

$$\ddot{r} = -r\cos\gamma - \dot{r}\sin\gamma - r\dot{\varphi}\cos\gamma. \tag{A.5}$$

The substitution of (A.2) and (A.5) into (A.1) and the use of (A.4) leads to

$$\dot{r} = h\left(r\cos\gamma, -r\sin\gamma\right)\sin\gamma \tag{A.6a}$$

$$\dot{\varphi} = h\left(r\cos\gamma, -r\sin\gamma\right)\frac{\cos\gamma}{r}. \tag{A.6b}$$

For $0 < \epsilon \ll 1$, $\dot{r}$ and $\dot{\gamma}$ are small. Therefore, r and φ vary much more slowly with t than $\gamma = t + \varphi$. Consequently, the Krylov-Bogoliubov approximation is used, i.e., Eq. (A.6) is averaged over the period 2π considering r, φ, $\dot{r}$ and $\dot{\varphi}$ are constant. That yields the following system

$$\dot{r} = \epsilon\frac{1}{8}r\left(4\sigma - \lambda r^2\right) \tag{A.7a}$$

$$\dot{\varphi} = 0 \tag{A.7b}$$

that approximates Eq. (A.6).

In this approximation, the phase φ is constant (and equal to the initial phase denoted as φ_0) and uncoupled from the amplitude r. The amplitude equation (A.7a) can be solved analytically as

$$r(t) = \frac{2\sqrt{\sigma} e^{\frac{\sigma t \epsilon}{2}}}{\sqrt{\frac{4\sigma}{r_0^2} + \lambda \left(e^{\sigma t \epsilon} - 1\right)}}, \tag{A.8}$$

where $r_0 = r(t = 0)$.

Appendix B. Expression of the regular non normally hyperbolic fixed point of the branch $\mathcal{M}_{02}$ of the critical manifold

Substituting the explicit expressions of the functions H_{01}, H_{02} and H_{03} and their derivative into Eq. (51) we obtain

$$\mathbf{J_g}(p_2) = \begin{pmatrix} \frac{3\alpha c^2 - 2\beta}{\mu} & \frac{3\sqrt{\alpha} c \sqrt{2\beta - 3\alpha c^2}}{\sqrt{2}\mu} & 0 \\ \frac{3\sqrt{2}\sqrt{\alpha} c \mu \sqrt{2\beta - 3\alpha c^2}}{\mu^2 + 4} & \frac{\mu\left(-8\beta + 9\alpha c^2 - 4\right)}{4(\mu^2 + 4)} & -\frac{c\left(-8\beta + 15\alpha c^2 + 2\mu^2 + 4\right)}{2(\mu^2 + 4)} \\ \frac{6\sqrt{2}\sqrt{\alpha}\sqrt{2\beta - 3\alpha c^2}}{\mu^2 + 4} & \frac{-8\beta + 9\alpha c^2 + 2\mu^2 + 4}{2c\mu^2 + 8c} & \frac{\mu\left(-8\beta + 15\alpha c^2 - 4\right)}{4(\mu^2 + 4)} \end{pmatrix} \tag{B.1}$$

whose third-order characteristic polynomial $p_{\mathbf{J_g}(p_2)}(z)$ has the following form

$$p_{\mathbf{J_g}(p_2)}(z) = a_0 z^3 + a_1 z^2 + a_2 z + a_3. \tag{B.2}$$

For such a third-order system, the Routh-Hurwitz stability criterion (see e.g. [36]) states that the roots of (B.2) have negative real parts if and only if the following inequalities

$$a_0 > 0, \quad a_1 > 0, \quad a_2 > 0, \quad a_3 > 0, \quad d_2 = a_1 a_2 - a_0 a_3 > 0 \tag{B.3}$$

are satisfied.

The coefficient a_i $(i = 0, \ldots, 3)$ and d_2 are plotted in Fig. B.13 as functions of c for the same parameters as used in Fig. 6. Comparing Figs. 7 and B.13 we deduce that the value of c corresponding to the regular non normally hyperbolic fixed point of the branch $\mathcal{M}_{02}$ of the critical manifold is one of the solutions of $d_2 = 0$.

The coefficient d_2 is a third-order polynomial with respect to $x = c^2$ with the following form

$$d_2 = b_1 x^3 + b_2 x^2 + b_3 x + b_4. \tag{B.4}$$

The roots of d_2 are computed by means of the Cardano's method (see e.g. [37]). First, the following parameters are introduced

$$p = -\frac{b_2^2}{3b_1^2} + \frac{c_3}{b_1}, \quad q = \frac{b_2}{27b_1}\left(\frac{2b_2^2}{b_1^2} - \frac{9b_3}{b_1}\right) + \frac{b_4}{b_1}.$$

The discriminant Δ is defined as $\Delta = -\left(4p^3 + 27q^2\right)$. Then:

1. If $\Delta < 0$, one root is real and two are complex conjugate.
2. If $\Delta = 0$, all roots are real and at least two are equal.
3. If $\Delta > 0$, all roots are real and unequal.

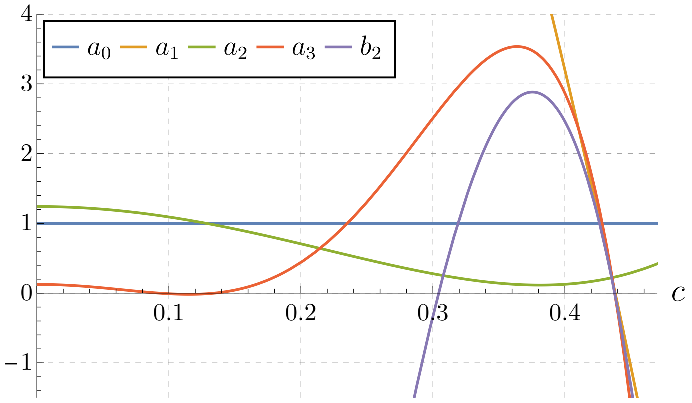

Figure B.13: The coefficients a_i ($i = 0, \dots, 3$) and d_2 are plotted in Fig. B.13 as functions of c for the same parameters as used in Fig. 6.

For the parameters used in this paper one has $\Delta > 0$. In this case, the three real roots x_k ($k = 0, 1, 2$) are given by

$$x_k = 2\sqrt{\frac{-p}{3}} \cos\left(\frac{1}{3} \arccos\left(\frac{3q}{2p}\sqrt{\frac{3}{-p}}\right) + \frac{2k\pi}{3}\right) - \frac{b_2}{3b_1}, \quad k = 0, 1, 2. \tag{B.5}$$

The wanted root is x_1. Then for the parameters used in Fig. 6 we obtain $c = \sqrt{x_1} = 0.325914$.

References

[1] O. V. Gendelman, L. I. Manevitch, A. F. Vakakis, R. M'Closkey, Energy Pumping in Nonlinear Mechanical Oscillators: Part I - Dynamics of the Underlying Hamiltonian Systems, Journal of Applied Mechanics 68 (1) (2001) 34. doi:10.1115/1.1345524.

[2] A. F. Vakakis, O. V. Gendelman, Energy pumping in nonlinear mechanical oscillators: Part II - Resonance capture, Journal of Applied Mechanics 68 (2001) 42–48.

[3] A. F. Vakakis, O. V. Gendelman, L. A. Bergman, D. M. McFarland, G. Kerschen, Y. S. Lee, Nonlinear Targeted Energy Transfer in Mechanical and Structural Systems, 1st Edition, no. 156 in Solid Mechanics and Its Applications, Springer, 2009.

[4] L. I. Manevitch, G. Sigalov, F. Romeo, L. A. Bergman, A. Vakakis, Dynamics of a linear oscillator coupled to a bistable light attachment: Analytical study, Journal of Applied Mechanics, Transactions ASME 81 (4) (2014) 1–10. doi:10.1115/1.4025150.

[5] F. Romeo, G. Sigalov, L. A. Bergman, A. F. Vakakis, Dynamics of a linear oscillator coupled to a bistable light attachment: Numerical study, Journal of Computational and Nonlinear Dynamics 10 (1) (2015) 1–13. doi:10.1115/1.4027224.

[6] M. A. Al-Shudeifat, Highly efficient nonlinear energy sink, Nonlinear Dynamics 76 (4) (2014) 1905–1920. doi:10.1007/s11071-014-1256-x.

[7] P. O. Mattei, R. Ponçot, M. Pachebat, R. Côte, Nonlinear targeted energy transfer of two coupled cantilever beams coupled to a bistable light attachment, Journal of Sound and Vibration 373 (2016) 29–51, publisher: Elsevier ISBN: 0022460X. doi:10.1016/j.jsv.2016.03.008.
URL http://dx.doi.org/10.1016/j.jsv.2016.03.008

[8] V. Iurasov, P. O. Mattei, Bistable nonlinear damper based on a buckled beam configuration, Nonlinear Dynamics 99 (3) (2020) 1801–1822, publisher: Springer. doi:10.1007/s11071-019-05387-7.

[9] F. Romeo, L. I. Manevitch, L. A. Bergman, A. Vakakis, Transient and chaotic low-energy transfers in a system with bistable nonlinearity, Chaos 25 (5), publisher: American Institute of Physics Inc. (May 2015). doi:10.1063/1.4921193.

[10] G. Habib, F. Romeo, The tuned bistable nonlinear energy sink, Nonlinear Dynamics 89 (2017) 179–196.

[11] K. Dekemele, P. Van Torre, M. Loccufier, Performance and tuning of a chaotic bi-stable NES to mitigate transient vibrations, Nonlinear Dynamics 98 (3) (2019) 1831–1851. doi:10.1007/s11071-019-05291-0.
URL http://link.springer.com/10.1007/s11071-019-05291-0

[12] Z. Wu, S. Seguy, M. Paredes, Estimation of Energy Pumping Time in Bistable Nonlinear Energy Sink and Experimental Validation, Journal of Vibration and Acoustics 144 (5) (2022) 051004. doi:10.1115/1.4054253.
URL https://asmedigitalcollection.asme.org/vibrationacoustics/article/144/5/051004/1139938/Estimation-of-Energy-Pumping-Time-in-Bistable

[13] Y. Wang, H. Yang, W. Song, C. Lu, Z. Liu, H. Zhou, Study on excitation threshold of strong modulation response and vibration suppression performance of bistable nonlinear energy sink, Journal of Vibration and Control (2023) 107754632311755doi:10.1177/10775463231175576.
URL http://journals.sagepub.com/doi/10.1177/10775463231175576

[14] Y. S. Lee, A. F. Vakakis, L. A. Bergman, D. M. McFarland, Suppression of limit cycle oscillations in the van der Pol oscillator by means of passive non-linear energy sinks, Structural Control and Health Monitoring 13 (1) (2006) 41–75. doi:10.1002/stc.143.

[15] O. V. Gendelman, T. Bar, Bifurcations of self-excitation regimes in a Van der Pol oscillator with a nonlinear energy sink, Physica D 239 (3-4) (2010) 220–229. doi:10.1016/j.physd.2009.10.020.

[16] Y. S. Lee, A. F. Vakakis, L. A. Bergman, D. M. McFarland, G. Kerschen, Suppression aeroelastic instability using broadband passive targeted energy transfers, part 1: Theory, AIAA Journal 45 (3) (2007) 693–711. doi:10.2514/1.24062.

[17] Y. S. Lee, A. F. Vakakis, L. A. Bergman, D. M. McFarland, G. Kerschen, Suppression aeroelastic instability using broadband passive targeted energy transfers, part 2: Experiments, AIAA Journal 45 (3) (2007) 2391–2400. doi:10.2514/1.24062.

[18] Y. S. Lee, A. F. Vakakis, D. M. Bergman, L. A. McFarland, G. Kerschen, Enhancing the robustness of aeroelastic instability suppression using multi-degree-of-freedom nonlinear energy sinks, AIAA Journal 46 (6) (2008) 1371–1394.

[19] O. V. Gendelman, A. F. Vakakis, L. A. Bergman, D. M. McFarland, Asymptotic analysis of passive nonlinear suppression of aeroelastic instabilities of a rigid wing in subsonic flow, SIAM Journal on Applied Mathematics 70 (5) (2010) 1655–1677. doi:10.1137/090754819.

[20] A. Luongo, D. Zulli, Aeroelastic instability analysis of nes-controlled systems via a mixed multiple scale/harmonic balance method, Journal of Vibration and Control 20 (13) (2014) 1985–1998. doi:10.1177/1077546313480542.

[21] B. Bergeot, Scaling law for the slow flow of an unstable mechanical system coupled to a nonlinear energy sink, Journal of Sound and Vibration 503 (2021) 116109. doi:10.1016/j.jsv.2021.116109.

[22] B. Bergeot, S. Bellizzi, S. Berger, Dynamic behavior analysis of a mechanical system with two unstable modes coupled to a single nonlinear energy sink, Communications in Nonlinear Science and Numerical Simulation 95 (2021) 105623. doi:10.1016/j.cnsns.2020.105623.

[23] B. Bergeot, Effect of stochastic forcing on the dynamic behavior of a self-sustained oscillator coupled to a non-linear energy sink, International Journal of Non-Linear Mechanics 150 (2023) 104351. doi:10.1016/j.ijnonlinmec.2023.104351.
URL https://linkinghub.elsevier.com/retrieve/pii/S0020746223000033

[24] G. R. Franzini, V. S. F. Maciel, G. J. Vernizzi, D. Zulli, Simultaneous passive suppression and energy harvesting from galloping using a bistable piezoelectric nonlinear energy sink, Nonlinear Dynamics (Sep. 2023). doi:10.1007/s11071-023-08888-8.
URL https://link.springer.com/10.1007/s11071-023-08888-8

[25] L. Manevitch, Complex representation of dynamics of coupled nonlinear oscillators, in: L. Uvarova, A. Arinstein, A. Latyshev (Eds.), Mathematical Models of Non-Linear Excitations, Transfer, Dynamics, and Control in Condensed Systems and Other Media, Springer US, 1999, pp. 269–300. doi:10.1007/978-1-4615-4799-0_24.

[26] A. Luongo, D. Zulli, Dynamic analysis of externally excited nes-controlled systems via a mixed multiple scale/harmonic balance algorithm, Nonlinear Dynamics 70 (2012) 2049–2061. doi:10.1007/s11071-012-0597-6.

[27] D. Zulli, A. Luongo, Control of primary and subharmonic resonances of a Duffing oscillator via non-linear energy sink, International Journal of Non-Linear Mechanics 80 (2016) 170–182. doi:10.1016/j.ijnonlinmec.2015.08.014.

[28] A. Nayfeh, Perturbation Methods, Physics textbook, Wiley, 2008.

[29] C. Jones, Geometric singular perturbation theory, in: R. Johnson (Ed.), Dynamical Systems, Vol. 1609 of Lecture Notes in Mathematics, Springer Berlin Heidelberg, 1995, pp. 44–118. doi:10.1007/BFb0095239.

[30] E. Domany, O. V. Gendelman, Dynamic responses and mitigation of limit cycle oscillations in van der pol-duffing oscillator with nonlinear energy sink, Journal of Sound and Vibration 332 (2013) 5489–5507.

[31] A. H. Nayfeh, Introduction to perturbation techniques, Wiley Classics Library, Wiley VCH, Weinheim, Germany, 2011.

[32] B. Bergeot, S. Bellizzi, Asymptotic analysis of passive mitigation of dynamic instability using a nonlinear energy sink network, Nonlinear Dynamics 94 (2) (2018) 1501–1522. doi:10.1007/s11071-018-4438-0.

[33] B. Bergeot, S. Bellizzi, Steady-state regimes prediction of a multi-degree-of-freedom unstable dynamical system coupled to a set of nonlinear energy sinks, Mechanical Systems and Signal Processing 131 (2019) 728–750.

[34] C. Kuehn, Multiple Time Scale Dynamics, 1st Edition, Vol. 191 of Applied Mathematical Sciences, Springer International Publishing, 2015.

[35] N. Berglund, B. Gentz, Berglund, Gentz - 2006 - Noise-induced phenomena in slow-fast dynamical systems a sample-paths approach, Springer London, 2006. doi:https://doi.org/10.1007/1-84628-186-5.

[36] F. Brauer, J. A. Nohel, The qualitative theory of ordinary differential equation: an introduction, Dover, New York, 1969.

[37] M. Spiegel, S. Lipschutz, J. Liu, Mathematical Handbook of Formulas and Tables (page 13), 4th Edition, McGraw-Hill, 2012. doi:10.1036/9780071795388.